

Hidden quasi-symmetries stabilize non-trivial quantum oscillations in CoSi

Chunyu Guo,^{1*} Lunhui Hu,^{2*} Carsten Putzke,¹ Jonas Diaz,¹ Xiangwei Huang,¹ Kaustuv Manna,^{3,4} Feng-Ren Fan,³ Chandra Shekhar,³ Yan Sun,³ Claudia Felser,³ Chaoxing Liu,^{2†} B. Andrei Bernevig,^{5,6,7†} Philip J. W. Moll^{1†}

¹Laboratory of Quantum Materials (QMAT), Institute of Materials (IMX), École Polytechnique Fédérale de Lausanne (EPFL), CH-1015 Lausanne, Switzerland

²Department of Physics, The Pennsylvania State University, University Park, PA, USA

³Max Planck Institute for Chemical Physics of Solids, 01187 Dresden, Germany

⁴Department of Physics, Indian Institute of Technology Delhi, New Delhi 110016, India

⁵Department of Physics, Princeton University, Princeton, New Jersey 08544, USA

⁶Donostia International Physics Center, P. Manuel de Lardizabal 4, 20018 Donostia-San Sebastian, Spain

⁷IKERBASQUE, Basque Foundation for Science, Bilbao, Spain

*These authors contributed equally to this work.

†Corresponding authors: cx156@psu.edu(C.X.L.); bernevig@princeton.edu(B.A.B.); philip.moll@epfl.ch(P.J.W.M.)

The symmetries of a crystal form the guiding principle to understand the topology of its band structure. They dictate the location and degrees of stable band crossings which lead to significant sources of Berry curvature. Here we show how non-crystalline quasi-symmetries stabilize near-degeneracies of bands over extended regions in energy and in the Brillouin zone. Specifically, a quasi-symmetry is an exact symmetry of a $k \cdot p$ Hamiltonian to lower-order that is broken by higher-order terms. Hence quasi-symmetric points are gapped,

yet the gap is parametrically small and therefore does not influence the physical properties of the system. We demonstrate that in the eV-bandwidth semi-metal CoSi an internal quasi-symmetry stabilizes gaps in the 1-2 meV range over a large near-degenerate plane. This quasi-symmetry is key to explaining the surprising simplicity of the experimentally observed quantum oscillations of four interpenetrating Fermi surfaces around the R-point. Untethered from limitations of crystalline symmetry, quasi-symmetries can source large Berry curvature over wide ranges of energy and on low symmetry points - thereby impacting quasiparticle dynamics in unexpected places. Quasi-symmetries also lead to new types of Wigner-Von Neumann classifications.

The introduction of concepts of topology in the past years into the field of electronic dispersions has captured the imagination of condensed matter physics and sparked a flurry of new research directions in the past years. At its core is the realization that the electronic waveforms constituting a material cannot always be derived from an entirely local description. In these topologically non-trivial metals, the wavefunctions are inherently non-local, and as such novel electronic states are expected and observed at the crystal surface terminating them (*1-10*). Beyond these surface properties, interesting anomalies in the bulk dispersion lead to novel physical phenomena, such as the emergence of quasiparticles mimicking ultra-relativistic Weyl- and Dirac-Fermions in 3D; a solid-state analogon of the Adler-Bell-Jackiw anomaly; a planar Hall effect; topological piezoelectric effect; second harmonic generation in Weyl semimetals; or strong Berry curvature that impacts the semi-classical and quantum dynamics of quasiparticles (*11-19*).

Given the wealth of new phenomena and potential applications, it is important to identify such "ideal" Weyl-, Dirac- or nodal-line semi-metals in which a priori unrelated chemical potential and the topological anomaly coincide. That such a coincidence is rather rare can be

understood from the Wigner-Von Neumann theorem, which states that a two-level crossing generally requires three tuning parameters (24, 25). Any two-level model can be expanded as $H = \epsilon_0 + \sum_i d_i \sigma_i$ where $i = x, y, z$ and ϵ_0 is an offset, while the momenta k_i take the role of the generic tuning parameters d_i in this discussion. Thus to obtain a two level degeneracy, all 3 tuning parameters are required to achieve $d_x = d_y = d_z = 0$ (codimension 3). Such a point would generally only coincide with the Fermi level accidentally. To stabilize crossings of more than two bands or achieve higher dimensional degeneracies (nodal lines, planes), additional crystalline symmetries must provide further constraints on the form of the Hamiltonian, such as two-fold screw axis for the nodal plane in MnSi (26) or rotational symmetries for the fourfold Dirac points in the 3D Dirac semi-metals Cd_3As_2 and Na_3Bi (6, 7). As symmetry and topology are inseparably intertwined, it is natural that symmetry should guide our search for interesting materials.

Here we refine this picture, and argue for the importance of approximate symmetries as an additional concept [Fig. 1(a)] that can generate interesting measurable quantum phenomena. A crystalline symmetry operation, M , commutes with the Hamiltonian of the system, $[H(k), M] = 0$. The well-known representation theory dictates that low-symmetry points, such as generic k-point in the Brillouin zone, usually support only one-dimensional representations, and hence bands anti-cross at these points. It may further be possible, however, that at these low symmetry points *approximate* symmetries emerge and can even be k-dependent. They are not exact symmetries of the material yet still commute with a dominant part of the Hamiltonian. Such approximate symmetries would stabilize almost linear band crossings by enforcing finite yet perturbatively small energy gaps. They already naturally occur when exact symmetries are weakly broken, such as tiny monoclinic distortions weakly removing a rotational symmetry that otherwise stabilizes a band crossing point. Graphene could be considered as an alternative example in the spin channel, as its Dirac point is weakly gapped when spin-orbit coupling is

considered, turning spin-rotation into an approximate symmetry (27). However, as approximate symmetries leave the bounds set by crystalline point-groups, more exciting hidden approximate symmetries may emerge that have no counterpart in the crystal symmetry. A famous example of a hidden symmetry is the Laplace–Runge–Lenz vector in classical gravitation. It is the conserved quantity stabilized by the hidden SO(4) symmetry of the r^{-1} potential of the Kepler problem that enforces strictly closed classical gravitational orbits. Weak perturbations, such as $r^{-1+\epsilon}$, mathematically reduce the symmetry to SO(3), yet the almost closed orbits for small ϵ evidence that the system senses the proximity to that hidden symmetry.

We adopt the term “quasi-symmetry” to denote a special type of approximate symmetry of electronic band structures, that emerges from the hierarchy of a $k \cdot p$ type of perturbation expansion around a high-symmetry point. Quasi-symmetries are operators M_{eff} that are the *exact* symmetries of the lower-order expansion but not of higher-order perturbation terms. The main goal of this paper is to show such a quasi-symmetry exists in the semi-metal CoSi as well as a large set of similar materials, and that it enforces a low-symmetry plane of near-degeneracies spanning the Brillouin zone which pin a source of Berry curvature to the Fermi level (Fig. 1). Excitingly, it falls into the latter category of hidden quasi-symmetries that are unrelated to approximate point-group symmetries, but can be treated as a symmetry of internal degrees of freedom, akin to spin in graphene. Unlike graphene, however, the form of quasi-symmetry is non-trivial as the corresponding symmetry operator is k -dependent and forms a part of the Hamiltonian. It has remarkable consequences on the quantum oscillation spectrum, which we here present as the first experimental observation of material properties critically defined by quasi-symmetries.

CoSi crystallizes in a chiral cubic structure of space group $P2_13$ without an inversion center [Fig. 2(a)]. Recent studies revealed the existence of exceptionally long Fermi arcs which connect the sixfold and fourfold band degenerate points (9, 29–31). These two degenerate points

correspond to two branches of Fermi surfaces located at the Γ - and R-point, respectively, yet only the R-point pockets are observed in quantum oscillation experiments. Band structure calculations reveal four split bands due to spin-orbit coupling which correspond to four Fermi surfaces at R, which we label as 1^+ , 1^- , 2^+ , 2^- , representing the orbital and spin degree of freedom respectively. States at the boundary of the Brillouin zone are doubly degenerate due to crystalline symmetry, hence the non-degenerate Fermi surfaces are enforced to touch there (5). The spin-orbit coupling and the orbital gap are both small yet similar in magnitude, which explains how four slightly degenerate, interpenetrating spheroids make up a surprisingly rich internal structure of the Fermi surfaces.

CoSi single crystals resemble octahedra, indicating a dominant growth along the [111] direction (see supplement for growth details). The quality of the single-phase crystallinity was checked by Laue and single crystal X-Ray diffraction. These crystals were fabricated into microstructures using focused-ion-beam machining (32) (see supplement) to increase the current path homogeneity and signal of Shubnikov-de Haas oscillations. The resistivity as well as the large residual resistivity ratio in the samples agrees well with previous bulk measurements (34), indicating an unchanged material quality during fabrication (Fig. 3). Hence not surprisingly, large quantum oscillations of the magnetoresistance are readily observed at low fields. Subtracting a polynomial background uncovers strong oscillations that resemble a beating pattern of two frequencies around $F_1 \sim 550$ T and $F_2 \sim 660$ T. These two, and their harmonics, are the only frequencies observed in our as well as previous experiments (33–36). The temperature dependence of the oscillations follows well the Lifshitz-Kosevich form, leading to a low cyclotron effective mass of $m_c \sim 0.84 m_e$.

In light of the complexity of the self-intersecting Fermi surfaces it appears at first surprising that the quantum oscillation spectrum is tantalizingly simple, with only two frequencies that, most importantly, only weakly depend on the direction of the applied magnetic field (Fig. 4).

When magnetic quantum oscillations arise from such highly degenerate Fermi surfaces, the main question is which, if any, possible trajectories become quantum coherent. As the Fermi-surface is centered around the R-point, any orbit necessarily crosses the symmetry-enforced degeneracies at the Brillouin zone boundary multiple times. This has been argued to stabilize band degeneracies pinned to the Fermi level in this crystal structure (26, 36) on the planes of Brillouin zone boundary [marked pink in Fig. 4(a)] .

Yet the orbits further intersect at low-symmetry points at which a gap must open [marked blue in Fig. 4(a)]. Neither the frequencies nor their angle dependence obtained from DFT calculations match the data if this gap is considered to separate the orbits via significant avoided-crossing. As the gap is small, the quasiparticle may tunnel across it continuing on the original trajectory, a phenomenon known as magnetic breakdown (37–40). Based on estimations of the gap from DFT and further analytical calculations, vanishingly small breakdown fields fall below 0.11 T for any field orientation, and hence the experimental data is always obtained in an extreme breakdown regime (see supplement for details). Thus the wavefunctions propagate through these points at perfect transmission, and indeed an excellent match of frequencies and their angle dispersion between theory and experiment is found (Fig. 4).

The oscillation spectrum thus can be completely rationalized a priori without quasi-symmetries. However one overlooks a key question about the structure of the wavefunctions, namely why in a metal with eV bandwidth two bands anti-cross with a gap no larger than 2 meV over the entire Fermi surface. To obtain such a parametrically small gap accidentally, an unreasonable degree of fine-tuning is required that acts simultaneously at many k-points, as well as at a wide range of energies as we will show. Instead, a hidden quasi-symmetry enforces the smallness of the gap at these points, and thus explains why magnetic breakdown at full transparency occurs at any arbitrary angle.

To understand this quasi-symmetry, we next consider an effective model around the R-point.

Without spin-orbit coupling (SOC), all the bands are eight-fold degenerate at R due to the combination of two-fold screw axis symmetries along the x and y direction and time reversal symmetry. Including spin doubles the degeneracy and the SOC splits the eight-fold degenerate states into six-fold and two-fold degenerate states at the R-point. An effective model for these eight bands around the R-point can be constructed as

$$\mathcal{H}_R = \mathcal{H}_0(\mathbf{k}) + \mathcal{H}_{soc} + \mathcal{H}_{k^2}(\mathbf{k}), \quad (1)$$

where $\mathcal{H}_0(\mathbf{k}) = C_0 + 2A_1(\mathbf{k} \cdot \mathbf{L})$ is the lower-order expansion of the spin-independent Hamiltonian, and three 4-by-4 matrices \mathbf{L} form an emergent angular momentum algebra $[L_i, L_j] = i\varepsilon_{ijk}L_k$ with Levi-Civita symbol ε_{ijk} and $i, j, k = x, y, z$. The SOC term is given by $\mathcal{H}_{soc} = 2\lambda_0(\mathbf{s} \cdot \mathbf{L})$, where \mathbf{s} is the spin operator. $\mathcal{H}_{k^2}(\mathbf{k})$ is the higher-order spin-independent term with its form given in the supplement. Here $\mathcal{H}_0(k) + \mathcal{H}_{k^2}(k)$ is the SOC-free expanded Hamiltonian to second order. By choosing appropriate parameters such as C_0, A_1, λ_0 , the energy dispersion of \mathcal{H}_R well reproduces that from the DFT calculations (see supplement).

A striking feature in the Hamiltonian \mathcal{H}_R is that the SOC term \mathcal{H}_{soc} takes a similar form as the linear-momentum term, just by replacing the momentum \mathbf{k} by spin \mathbf{s} . This is because spin, as a pseudo-vector, behaves exactly the same as a vector due to the lack of inversion, mirror or other roto-inversion symmetries for a chiral crystal. Due to this similarity, up to the first-order perturbation, we find that the spin of the eigen-states is parallel or anti-parallel to the momentum \mathbf{k} and thus we can label the spin states of these bands by \pm in Fig. 1(e). We derive an effective Hamiltonian for the near degenerate bands. This can be done by first projecting the full Hamiltonian \mathcal{H}_R into the 4 closest bands (1^\pm and 2^\pm bands) to get a 4-band model and then constructing a 2-band model for the 1^- and 2^+ bands, as discussed in supplement. Up to the first-order perturbation, the 2-band Hamiltonian takes the form $H_{eff} = \epsilon_0 + d_z(\mathbf{k})\sigma_z$, where $d_z(\mathbf{k}) = \lambda_0 - \sqrt{3}\tilde{C}'\frac{|k_x k_y k_z|}{k}$ and the form of the function ϵ_0 is given in supplement. Here σ_z is the

Pauli matrix on the basis of 1^- and 2^+ bands, λ_0 term comes from the SOC Hamiltonian \mathcal{H}_{soc} and the \tilde{C} term from $\mathcal{H}_{k^2}(\mathbf{k})$. It is striking to see that the operator $\mathcal{M}_{eff} = \sigma_z$ commutes with H_{eff} and thus serves as an *exact* symmetry at the first-order expansion. The existence of \mathcal{M}_{eff} forbids any terms that are coupled to $\sigma_{x,y}$ in the effective Hamiltonian, thus reducing the codimension of a two-level crossing from 3 to 1 and stabilizing a nodal plane, which is defined by the equation $\lambda_0 = \sqrt{3}\tilde{C}\frac{|k_x k_y k_z|}{k}$ in this two-band model. A more accurate and complete description around the Fermi energy is the 4-band model, which shares a similar k-dependent hidden quasi-symmetry and is essential in deriving the 2-band model (see supplement), and the whole perturbation theory reveals a striking hierarchy structure (41). Higher-order perturbation expansion breaks \mathcal{M}_{eff} through inducing additional terms coupled to $\sigma_{x,y}$ in the effective model and thus leads to a small gap opening of this nodal plane (See supplement). Therefore, \mathcal{M}_{eff} is not a symmetry of the system, but an emergent quasi-symmetry in the sense of low-energy effective theory. Importantly, this curved nodal plane spans low-symmetry regions of the Brillouin zone, in contrast to symmetry-enforced exact degeneracies. It is this combined structure of symmetry and quasi-symmetry induced degeneracies that forms the basis of the complex structure of the Fermi surface centered at R, and reduces the complexity of the quantum orbits in magnetic fields to two, angle-independent frequencies.

Compared to the exact degeneracy due to symmetry, near degeneracies from quasi-symmetry have unique implications in the Berry curvature distribution in momentum space [Fig. 1(e)]. The U(1) Berry curvature is not well-defined at a degeneracy, while for near-degeneracy, the small gap concentrates significant Berry curvature. In our model, the Berry curvature almost vanishes in the vicinity of the exact degenerate plane, yet it is concentrated to a ring on the near nodal plane at any fixed energy. This large Berry curvature around the near nodal lines, which always occurs at the Fermi energy, may strongly affect physical phenomena that are related to local Berry curvature, including intrinsic spin Hall effect (42, 43) and quantum non-

linear Hall effect (44). The strong Berry curvature is focused into the near-degeneracy, where the quasiparticle tunneling occurs. It will be interesting to explore how this Berry curvature modifies the tunneling conditions in magnetic breakdowns at such quasi-symmetry given near-degeneracies (45).

The observation of quasi-symmetries raises new questions on how wave functions can be woven together in condensed matter systems. The most practical concerns finding the main ingredients for quasi-symmetries to occur in actual materials. The novelty of separating them from crystalline symmetries equally presents a challenge in that a detailed and rigorous analysis of the electronic bands at all low-symmetry k-points is required to identify them. Search programs based on symmetry analysis will not find this type of anomaly without further guideline. It is natural, however, to suspect related compounds crystallizing in the same structure to share this feature, such as e.g. PtGa, PtAl, RhSi and the magnetic MnSi where the influence of magnetism can be explored. (26, 46–54). At the same time, it raises the interesting prospect that even those materials in which crystalline symmetries do not allow stable band crossings may still host exotic quasiparticles and strong Berry curvature at the Fermi level due to the hidden proximity of the system to a topological state. Here, quantum oscillation experiments may provide guidance by pointing to materials with similarly extreme magnetic breakdown on extended regions on the Fermi surface, which a quasi-symmetry would naturally explain without further fine-tuning. On the theoretical side, it will be critical to elucidate further the physical meaning of the M_{eff} in CoSi and to evolve the understanding of the mathematical structure behind it. These developments are expected to hold an interesting future for the role of topology. A consensus of high-throughput efforts emerges that 20-30% of materials are topological (20–23). Yet it appears that crystal symmetry may not hold up as the strict barrier it was thought to be, and via quasi-symmetries concepts of topology may reach even further than these estimates predict.

References

1. Armitage, N. P., Mele, E. J., and Vishwanath, A., Weyl and Dirac semimetals in three-dimensional solids. *Rev. Mod. Phys.* **90**, 015001 (2018).
 2. Lv, B. Q., Qian, T., and Ding, H., Experimental perspective on three-dimensional topological semimetals. *Rev. Mod. Phys.* **93**, 025002 (2021).
 3. Wan, X. G., Turner, A. M., Vishwanath, A., and Savrasov, S. Y., Topological semimetal and Fermi-arc surface states in the electronic structure of pyrochlore iridates. *Phys. Rev. B* **83**, 205101 (2011).
 4. Wang, Z., Alexandradinata, A., Cava, R. J., and Bernevig, B. A., Hourglass fermions. *Nature* **532**, 7598 (6).
 5. Bradlyn, B., Cano, J., Wang, Z., Vergniory, M. G., Felser, C., Cava, R. J., and Bernevig, B. A., Beyond Dirac and Weyl fermions: Unconventional quasiparticles in conventional crystals. *Science* **353**, aaf5037 (2016).
 6. Wang, Z., Sun, Y., Chen, X.-Q., Franchini, C., Xu, G., Weng, H., Dai, X., and Fang, Z., Dirac semimetal and topological phase transitions in $A_3\text{Bi}$ ($A=\text{Na, K, Rb}$). *Phys. Rev. B* **85**, 195320 (2012).
 7. Wang, Z., Weng, H., Wu, Q., Dai, X., and Fang, Z., Three-dimensional Dirac semimetal and quantum transport in Cd_3As_2 . *Phys. Rev. B* **88**, 125427 (2013).
- Titus
8. Bian, G., Chang, T., Zheng, H., Velury, S., Xu, S.-Y., and Neupert, T. et al., Drumhead surface states and topological nodal-line fermions in TlTaSe_2 . *Phys. Rev. B* **93**, 121113 (2016).

9. Rao, Z., Li, H., Zhang, T., Tian, S., Li, C., and Fu, B. et al., Observation of unconventional chiral fermions with long Fermi arcs in CoSi. *Nature* **567**, 496 (2019).
10. Moll, P. J. W., Nair, N. L., Helm, T., Potter, A. C., Kimchi, I., Vishwanath, A., and Analytis, J. G., Transport evidence for Fermi-arc-mediated chirality transfer in the Dirac semimetal Cd_3As_2 . *Nature* **535**, 266 (2016).
11. Zyuzin, A. A., and Burkov, A. A., Topological response in Weyl semimetals and the chiral anomaly. *Phys. Rev. B* **86**, 115133 (2012).
12. Burkov, A. A., Chiral anomaly and transport in Weyl metals. *J. Condens. Matter Phys.* **27**, 113201 (2015).
13. Xiong, J., Kushwaha, S. K., Liang, T., Krizan, J. W., Hirschberger, M., and Wang, W., et al., Evidence for the chiral anomaly in the Dirac semimetal Na_3Bi . *Science* **350**, 413 (2015).
14. Matsushita, T., Fujimoto, S., and Schnyder, A. P., Topological piezoelectric effect and parity anomaly in nodal line semimetals. *Phys. Rev. Research* **2**, 043311 (2020).
15. Li, Z., Jin, Y.-Q., Tohyama, T., Iitaka, T., Zhang, J.-X., and Su, H., Second harmonic generation in the Weyl semimetal TaAs from a quantum kinetic equation. *Phys. Rev. B* **97**, 085201 (2018).
16. Takasan, K., Morimoto, T., Orenstein, J., and Moore, J. E., Current-induced second harmonic generation in inversion-symmetric Dirac and Weyl semimetals. *arXiv: 2007.08887* (2020).
17. Burkov, A. A., Giant planar Hall effect in topological metals. *Phys. Rev. B* **96**, 041110 (2017).

18. Liu, E., Sun, Y., Kumar, N., Muechler, L., Sun, A., and Jiao, L. et al., Giant anomalous Hall effect in a ferromagnetic kagome-lattice semimetal. *Nat. Phys.* **14**, 1125 (2018).
19. Nakatsuji, S., Kiyohara, N., and Higo, T., Large anomalous Hall effect in a non-collinear antiferromagnet at room temperature. *Nature* **527**, 212 (2015).
20. Bradlyn, B., Elcoro, L., Cano, J., Vergniory, M., Wang, Z., Felser, C., Aroyo, M., and Bernevig, B. A., Topological quantum chemistry. *Nature* **547**, 298 (2017).
21. Zhang, T., Jiang, Y., Song, Z., Huang, H., He, Y., Fang, Z., Weng, H., and Fang, C., Catalogue of topological electronic materials. *Nature* **566**, 475 (2019).
22. Vergniory, M. G., Elcoro, L., Felser, C., Bernevig, B. A., and Wang, Z., A complete catalogue of high-quality topological materials. *Nature* **566**, 480 (2019).
23. Tang, F., Po, H. C., Vishwanath, A., and Wan, X. G., Comprehensive search for topological materials using symmetry indicators. *Nature* **566**, 486 (2019).
24. von Neumann, V. J., and Wigner, E., Uber merkwürdige diskrete Eigenwerte. *Phys. Z.* **30**, 465 (1929).
25. Murakami, S., Iso, S., Avishai, Y., Onoda, M., and Nagaosa, N., Tuning phase transition between quantum spin Hall and ordinary insulating phases. *Phys. Rev. B* **76**, 205304 (2007).
26. Wilde, M. A., Dodenhöft, M., Niedermayr, A., Bauer, A., Hirschmann, M. M., and Alpin, K. et al., Symmetry-enforced topological nodal planes at the Fermi surface of a chiral magnet. *Nature* **594**, 374 (2021).
27. Konschuh, S., Gmitra, M., and Fabian, J., Tight-binding theory of the spin-orbit coupling in graphene. *Phys. Rev. B* **82**, 245412 (2010).

28. Sichau, J., Prada, M., Anlauf, T., Lyon, T. J., Bosnjak, B., Tiemann, L., and Blick, R. H., Resonance Microwave Measurements of an Intrinsic Spin-Orbit Coupling Gap in Graphene: A Possible Indication of a Topological State. *Phys. Rev. Lett.* **122**, 046403 (2019).
29. Yuan, Q. Q., Zhou, L., Rao, Z. C., Tian, S., Zhao, W. M., and Xue, C. L. et al., Quasiparticle interference evidence of the topological Fermi arc states in chiral fermionic semimetal CoSi. *Science advances* **5**, eaaw9485 (2019).
30. Sanchez, D. S., Belopolski, I., Cochran, T. A., Xu, X., Yin, J. X., and Chang, G. Q., et al., Topological chiral crystals with helicoid-arc quantum states. *Nature* **567**, 500 (2019).
31. Fang, C., Gilbert, M. J., Dai, X., and Bernevig, B. A., Multi-Weyl topological semimetals stabilized by point group symmetry. *Phys. Rev. Lett.* **108**, 266802 (2012).
32. Moll, P. J. W., Focused Ion Beam Microstructuring of Quantum Matter. *Annu. Rev. Condens. Matter Phys.* **9**, 147 (2018).
33. Wu, D. S., Mi, Z. Y., Li, Y. J., Wu, W., Li, P. L., and Song, Y. T., et al., Single Crystal Growth and Magnetoresistivity of Topological Semimetal CoSi. *Chin. Phys. Lett.* **36**, 077102 (2019).
34. Xu, X., Wang, X., Cochran, T. A., Sanchez, D. S., Chang, G., and Belopolski, I. et al., Crystal growth and quantum oscillations in the topological chiral semimetal CoSi. *Phys. Rev. B* **100**, 045104 (2019).
35. Wang, H., Xu, S., Lu, X. Q., Wang, X. Y., Zeng, X. Y., and Lin, J. F. et al., de Haas–van Alphen quantum oscillations and electronic structure in the large-Chern-number topological chiral semimetal CoSi. *Phys. Rev. B* **102**, 115129 (2020).

36. Huber, N., Alpin, K., Causer, G. L., Worch, L., Bauer, A., Benka, G. et al., Network of topological nodal planes, multifold degeneracies, and Weyl points in CoSi. arXiv **2107.02820** (2021).
37. Blount, E. I., Bloch Electrons in a Magnetic Field. Phys. Rev. **126**, 1636 (1962).
38. Helm, T., Kartsovnik, M. V., Proust, C., Vignolle, B., Putzke, C., Kampert, E., et al., Correlation between Fermi surface transformations and superconductivity in the electron-doped high- T_c superconductor $\text{Nd}_{2-x}\text{Ce}_x\text{CuO}_4$. Phys. Rev. B **92**, 094501 (2015).
39. Honold, M. M., Harrison, N., Nam, M.-S., Singleton, J., Mielke, C. H., Kurmoo, M., and Day, P., Magnetic breakdown in the high-field phase of the organic conductor α -(BEDT-TTF) $_2$ KHg(SCN) $_4$. Synth. Met. **103**, 2093 (1999).
40. Pezzini, S., van Delft, M. R., Schoop, L. M., Lotsch, B. V., Carrington, A., Katsnelson, M. I., Hussey, N. E., and Wiedmann, S. et al., Unconventional mass enhancement around the Dirac nodal loop in ZrSiS. Nat. Phys. **14**, 178 (2017).
41. Hu, L. H., Guo, C. Y., Putzke, C., Diaz, J., Huang, X. W., Manna, K., Fan, F. -R., Shekhar, C., Sun, Y., Felser, C., Moll, P. J. W., Liu, C. X., Bernevig, B. A., (unpublished).
42. Sun, Y., Zhang, Y., Liu, C. X., Felser, C., and Yan, B., Dirac nodal lines and induced spin Hall effect in metallic rutile oxides. Phys. Rev. B **95**, 235104 (2017).
43. Sun, Y., Zhang, Y., Felser, C., and Yan, B., Strong intrinsic spin Hall effect in the TaAs family of Weyl semimetals. Phys. Rev. Lett. **117**, 146403 (2016).
44. Sodemann, I. and Fu, L., Quantum Nonlinear Hall Effect Induced by Berry Curvature Dipole in Time-Reversal Invariant Materials. Phys. Rev. Lett. **115**, 216806 (2015).

45. Wang, C., Duan, W., Glazman, L., and Alexandradinata, A., Landau quantization of nearly degenerate bands and full symmetry classification of Landau level crossings. *Phys. Rev. B.* **100**, 014442 (2019).
46. Yao, M., Manna, K., Yang, Q., Fedorov, A., Voroshnin, V., and Schwarze, B. V. et al., Observation of giant spin-split Fermi-arc with maximal Chern number in the chiral topological semimetal PtGa. *Nat. Comms.* **11**, 1 (2020).
47. Ma, J. Z., Wu, Q. S., Song, M., Zhang, S.-N., Guedes, E. B. and Ekahana, S. A. et al., Observation of a singular Weyl point surrounded by charged nodal walls in PtGa. *Nat. Comms.* **12**, 3994 (2021).
48. Xu, S., Zhou, L., Wang, X.Y., Wang, H., Lin, J.F., Zeng, X.Y., Cheng, P., Weng, H. and Xia, T.L., Quantum Oscillations and Electronic Structure in the Large-Chern-Number Topological Chiral Semimetal PtGa. *Chin. Phys. Lett.* **37**, 107504 (2020).
49. Schröter, N. B. M., Pei, D., Vergniory, M. G., Sun, Y, Manna, K., and de Juan, F. et al., Chiral topological semimetal with multifold band crossings and long Fermi arcs. *Nat. Phys.* **15**, 579 (2019).
50. Schröter, N. B. M., Stolz, S., Manna, K., de Juan, F., Vergniory, M. G., and Krieger J. A. et al., Observation and control of maximal Chern numbers in a chiral topological semimetal. *Science* **369**, 179 (2020).
51. Sessi, P., Feng-ren, F., Küster, F., Manna, K., and Vergniory, M. G. et al., Handedness-dependent quasiparticle interference in the two enantiomers of the topological chiral semimetal PdGa. *Science* **369**, 179 (2020).

52. Chang, G., Xu, S. Y., Wieder, B. J., Sanchez, D. S., Huang, S. M., and Belopolski, I. et al., Unconventional chiral fermions and large topological Fermi arcs in RhSi. *Phys. Rev. Lett.* **119**, 206401 (2017).
53. Rees, D., Manna, K., Lu, B., Morimoto, T., Borrmann, H., and Felser, C. et al., Helicity-dependent photocurrents in the chiral Weyl semimetal RhSi. *Sci. Adv.* **6**, eaba0509 (2020).
A. Rosch, A.
54. Mühlbauer, S., Binz, B., Jonietz, F., Pfleiderer, C., Rosch, A., and Neubauer, A. et al., Skyrmion Lattice in a Chiral Magnet. *Science* **323**, 915 (2009).

Acknowledgements:

Funding: This work was funded by the European Research Council (ERC) under the European Union's Horizon 2020 research and innovation programme (MiTopMat - grant agreement No. 715730). This project received funding by the Swiss National Science Foundation (Grants No. PP00P2.176789). C. X. Liu and L. H. Hu are supported by the Office of Naval Research (Grant No. N00014-18-1-2793) and Kaufman New Initiative research Grant No. KA2018-98553 of the Pittsburgh Foundation. K.M., and C.F. acknowledge the financial support from the European Research Council (ERC) Advanced Grant No. 742068 "TOP-MAT"; European Union's Horizon 2020 research and innovation program (Grant Nos. 824123 and 766566) and Deutsche Forschungsgemeinschaft (DFG) through SFB 1143. Additionally, K. M. acknowledges Max Plank Society for the funding support under Max Plank-India partner group project. B.A.B. thanks funding from the European Research Council (ERC) under the European Union's Horizon 2020 research and innovation programme (grant agreement no. 101020833). B.A.B. is also supported by the U.S. Department of Energy (Grant No. DE-SC0016239), and partially supported by the National Science Foundation (EAGER Grant No. DMR 1643312), a Simons Investigator grant (No. 404513), the Office of Naval Research (ONR Grant No. N00014-20-1-2303), the Packard Foundation, the Schmidt Fund for Innovative Research, the BSF Israel US foundation (Grant No. 2018226), the Gordon and Betty Moore Foundation through Grant No. GBMF8685 towards the Princeton theory program, and a Guggenheim Fellowship from the John Simon Guggenheim Memorial Foundation. B.A.B. is supported by the NSF-MERSEC (Grant No. MERSEC DMR 2011750). B.A.B. gratefully acknowledge financial support from the Schmidt DataX Fund at Princeton University made possible through a major gift from the Schmidt Futures Foundation. B.A.B. received additional support from the Max Planck Society. Further support was provided by the NSF-MRSEC No. DMR-1420541, BSF Israel US foundation No. 2018226, and the Princeton Global Network Funds.

Competing Interests The authors declare that they have no competing financial interests.

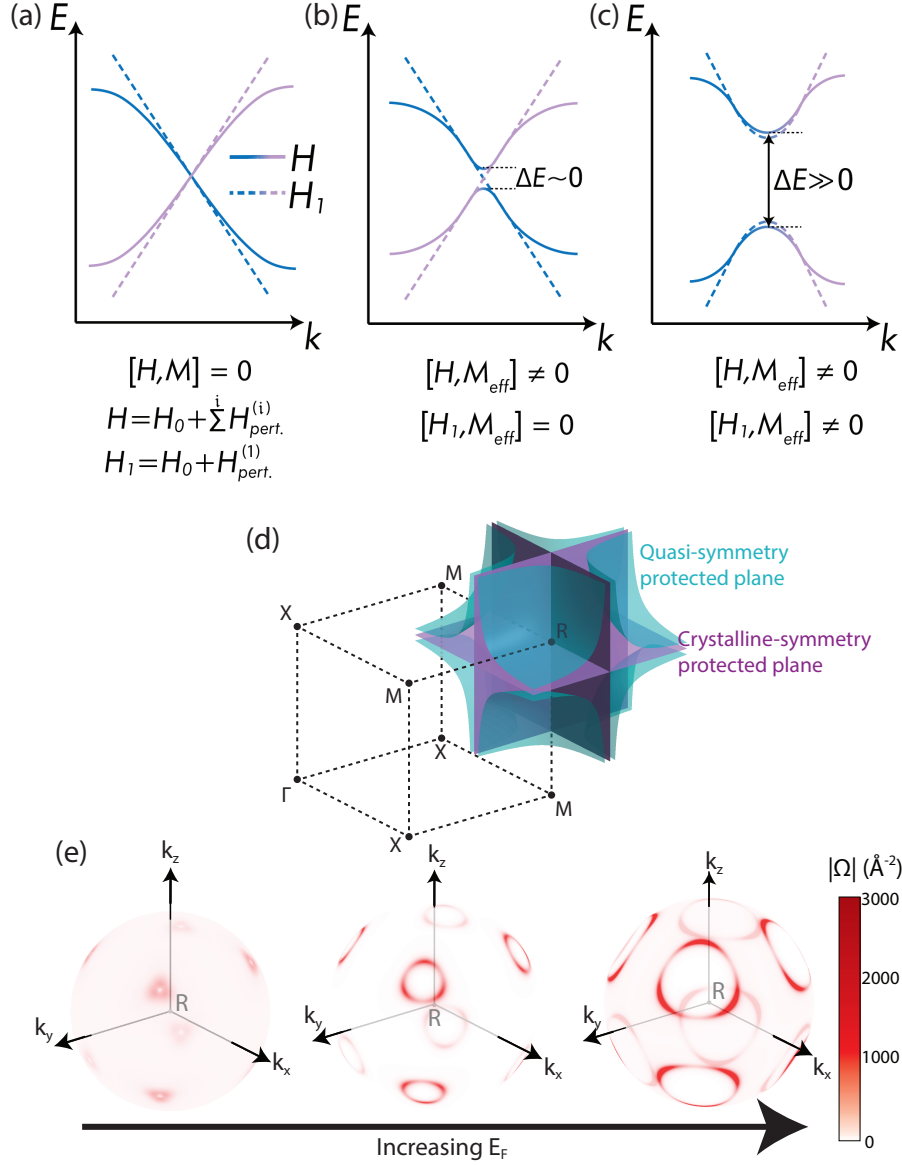


Figure 1: Illustration of quasi-symmetry. (a) If a crystalline symmetry operation commutes with the Hamiltonian system, the band crossing point is therefore symmetry-protected. (b) In this case the Hamiltonian itself does not commute with the symmetry operation yet its first order perturbation does. This lead to the situation where though the band crossing is numerically avoided but the resulted gap size is negligible for the physical properties of the system. This type of symmetry is called quasi-symmetry. (c) If the symmetry operation does not commute with the Hamiltonian to any order of perturbation of the system, the crossing is not protected by any symmetry. This will result in a sizeable gap and lost of topological character. (d) Quasi-symmetry and crystalline-symmetry protected degenerate planes. (e) The Berry curvature distribution of the 1^- -band [see Fig. 2(e)] at different Fermi energy calculated from the model Hamiltonian Eq. (1).

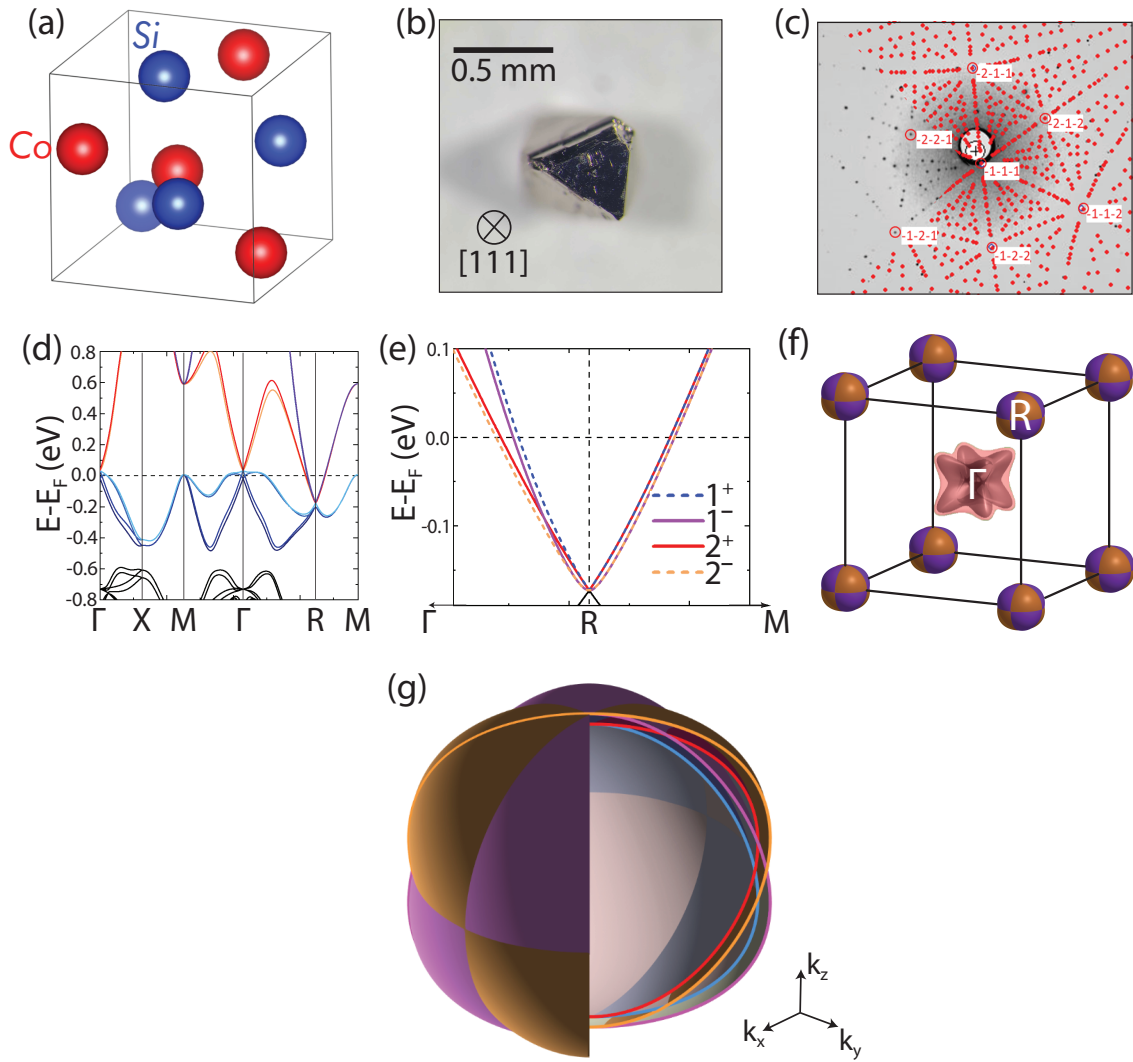


Figure 2: (a) Crystal structure of CoSi. Co and Si atoms are presented as red and blue spheres respectively. (b) Optical microscope image of a CoSi single crystal sample. (c) Laue diffraction pattern of the grown CoSi single crystal, superimposed with a theoretically simulated one confirming high crystalline quality. (d) Ab-initio-calculated band structure of CoSi. (e) Enlarged section of band structure around R-point. Here 1/2 denotes orbital character while +/- stands for the spin character of the band. (f) 3D view of all Fermi surfaces, which are centered around either R- or Γ - point of the Brillouin zone. (g) 3D view of Fermi surfaces centered around R-point with a quadrant cut.

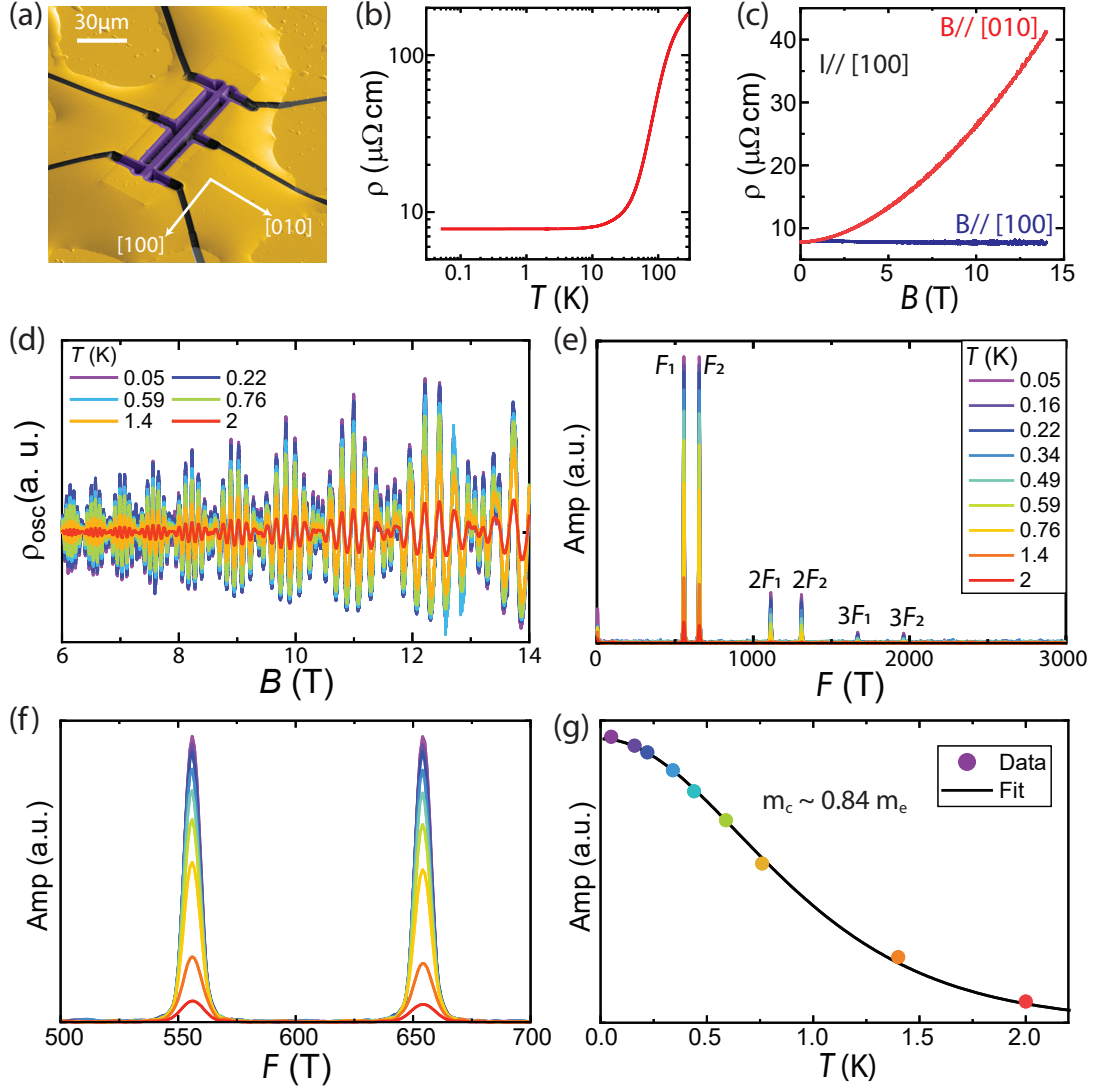


Figure 3: (a) Scanning electron microscope image of CoSi microdevice. A long bar along [100] direction with a 6 by 6 μm^2 cross section is fabricated by FIB. (b) Temperature dependence of resistivity measured from 300 K to 50 mK. (c) Transverse and longitudinal magnetoresistivity as a function of magnetic field. (d) Temperature-dependent SdH oscillations with field applied along [100] axis. Here $\rho_{osc} = \Delta\rho/\rho_{BG}$, with $\Delta\rho$ the oscillatory part of the magnetoresistivity, and ρ_{BG} the background obtained from a 3rd-order polynomial fit to the magnetoresistivity. (e) Fast-Fourier-transformation spectrum of the SdH oscillations presented in (d) with the field window of 3 to 14 T. Two main peaks, as well as their higher-harmonic components, can be clearly observed. The suppression of peak amplitude with increasing temperature is due to the thermal damping effect. (f) Lifshitz-Kosevich fit to the temperature dependence of cyclotron mass. The fitting yields a cyclotron mass $m_c \sim 0.84 m_e$, comparable to the previously reported values (34–36).

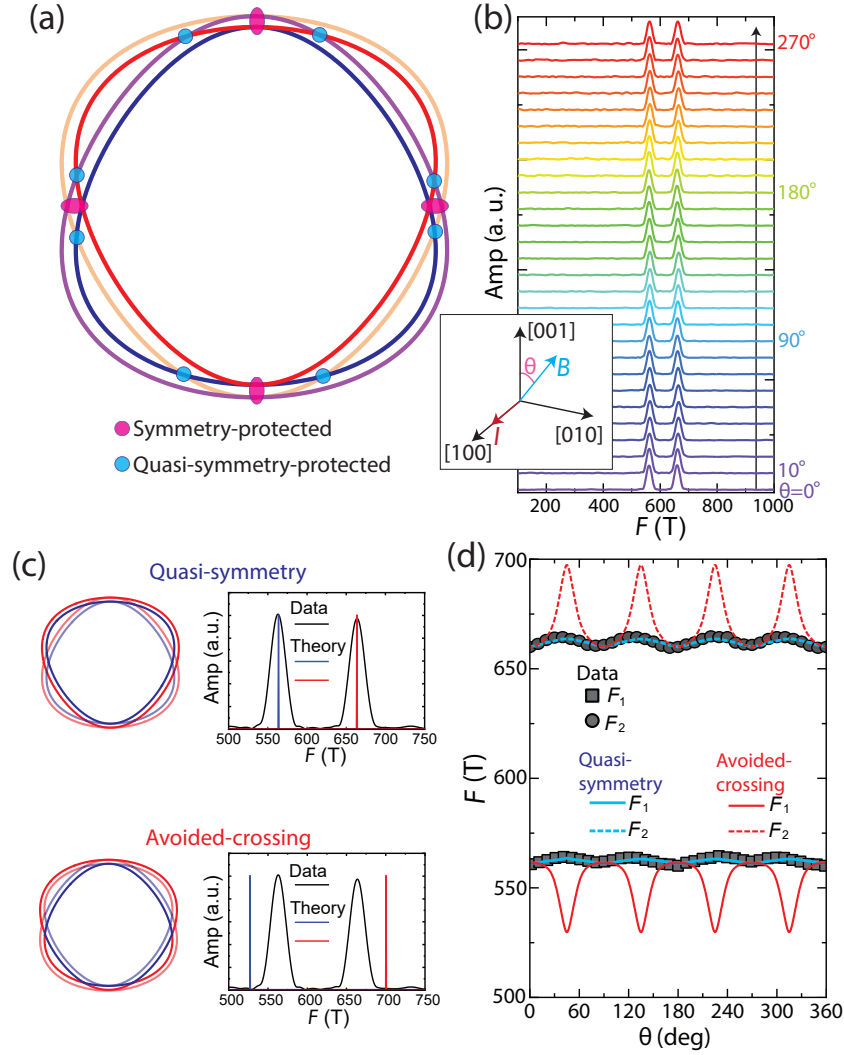


Figure 4: (a) (011) -orbit with symmetry-protected (pink) and quasi-symmetry protected (blue) degenerate points encircled. The symmetry-protected degenerate points always locate at the high symmetry plane while the quasi-symmetry protected crossings are positioned at arbitrary low-symmetry point. (b) Fast-fourier-transformation spectrum of angle-dependent quantum oscillations measured at $T = 2$ K. Here the magnetic field is rotated within (100) plane and the angle is defined between the field direction and $[001]$ axis. (c) Landau orbits and corresponding FFT spectrum for Quasi-symmetry and avoided-crossing scenarios. It is clear that only the quasi-symmetry scenario reproduces FFT peaks that match perfectly well with the experimental data. For the avoided crossing case the predicted frequency is far off. (d) Summary of angular dependence of oscillation frequencies. The contrast between two different scenario again clearly demonstrates that quasi-symmetry is the only option to explain the experimental results of nearly angle-independent oscillation frequencies.

Supplementary materials for "Hidden quasi-symmetries stabilize non-trivial quantum oscillations in CoSi"

Chunyu Guo*,¹ Lunhui Hu*,² Carsten Putzke,¹ Jonas Diaz,¹ Xiangwei Huang,¹
Kaustuv Manna,^{3,4} Feng-Ren Fan,³ Chandra Shekhar,³ Yan Sun,³ Claudia
Felser,³ Chaoxing Liu^{†,2}, B. Andrei Bernevig^{†,5,6,7} and Philip J. W. Moll^{†1}

¹*Laboratory of Quantum Materials (QMAT), Institute of Materials (IMX),
École Polytechnique Fédérale de Lausanne (EPFL), CH-1015 Lausanne, Switzerland*

²*Department of Physics, The Pennsylvania State University, University Park, PA, USA*

³*Max Planck Institute for Chemical Physics of Solids, 01187 Dresden, Germany*

⁴*Department of Physics, Indian Institute of Technology Delhi, New Delhi 110016, India*

⁵*Department of Physics, Princeton University, Princeton, New Jersey 08544, USA*

⁶*Donostia International Physics Center,*

P. Manuel de Lardizabal 4, 20018 Donostia-San Sebastian, Spain

⁷*IKERBASQUE, Basque Foundation for Science, Bilbao, Spain*

(Dated: August 10, 2021)

I. EXPERIMENTAL AND THEORETICAL METHODS

A. Single crystal growth

CoSi single crystals were grown in Te-flux. The high purity starting materials Co (99.95%, Alfa Aesar), Si (99.999%, Chempur) and Te (99.9999%, Alfa Aesar) were mixed in the molar ratio of 1:1:20. All materials were kept in a cylindrical alumina crucible and sealed in a quartz tube. The entire assembly was heated to 1050 °C at a rate of 100 °C/h, and held there for 15 h to ensure a homogeneous mixture. Successively, the sample was cooled to 700 °C at a rate of 2 °C/h, and extra Te-flux was removed by centrifugation at 700 °C. High quality CoSi single crystals in the mm-range resulted from this growth protocol.

B. Focused-ion-beam (FIB) microstructuring

$100 \times 40 \times 2 \mu\text{m}$ thin slabs were cut out from a CoSi single crystal via a FEI Helios Plasma FIB using Xe-ions. The lamella was then transferred to a sapphire substrate ex-situ with a micro-manipulator and glued down with the red araldite epoxy. After that it was structured to the designed geometry with the Plasma FIB.

C. Details of ab-initio band structure calculation

Electronic band structures of CoSi were calculated by density functional theory (DFT) using the full-potential local-orbital code (FPLO)¹ with a localized atomic basis and full potential treatment. The exchange and correlation energies were considered in the generalized gradient approximation level². To calculate the Fermi surface, we projected Bloch states onto high symmetric atomic-orbital-like Wannier functions and constructed tight-binding model Hamiltonian.

II. DETAILED ANALYSIS OF FERMI SURFACES AT R-POINT

A. Fermi surface Identity

Following the band character identification in band structure calculations [Fig. 2(d)] presented in the main manuscript, the four corresponding Fermi surfaces are also labelled as 1^+ , 1^- , 2^+

and 2^- (Fig. S1). Here 1 and 2 denote the orbit character while +/- stand for the spin character. Note that the sizes of 1- and 2- Fermi surfaces are larger than their spin-opposite counterpart due to spin-orbit-coupling as discussed in Sec. II C. For the clarification we separate them into two pairs: $1^+/2^+$ and $1^-/2^-$. Due to crystalline symmetry, these Fermi surfaces intersect exactly at the Brillouin zone boundary.

B. Slice-and-view of Fermi surfaces

To further demonstrate the Fermi surface geometry, the slice-and-view of the four Fermi surfaces is displayed in Fig. S2. As slicing from the top to the bottom of the Fermi surfaces, the slice section changes from ellipsoidal to circular and then back to ellipsoidal. Note that the ellipsoids from the top and bottom slice are elongated along orthogonal directions. This orthogonality is generally true for all Fermi surfaces [Fig. S2 (a) and (b)]. The combination of all sliced orbits, as displayed in Fig. S2 (c), show both crossings at the high symmetry plane and crossings protected by quasi-symmetry.

The Fermi surface orbits with field applied along different directions are shown in Fig. S3 (b) which demonstrate the evolution of degeneracies at the Fermi surfaces. For all four field directions displayed, the Fermi surface orbits are intersecting at multiple k-points. Degeneracies occur at the Brillouin zone boundary are protected by crystalline symmetry, while the others located at low symmetry k-points are formed due to quasi-symmetry. These two different types of degeneracies are denoted with different colors on Fig. S3 (b). The momentum difference from R-point Δk as a function of angle ϕ with different applied field directions is presented in Fig. S3 (c) with ϕ defined in S3 (b). Two different types of degenerate points are marked with pink and blue circle respectively.

C. Influence of spin-orbit-coupling

In this section, we discuss the influence of spin-orbit-coupling (SOC) on band structure. Without SOC, the spin degeneracy is preserved and therefore all bands are at least two-fold degenerate throughout the Brillouin zone. At the boundary of the Brillouin zone, the crystalline symmetry enforces a four-fold band degeneracy, as revealed by the ab-initio band structure calculation [Fig. S4 (a)]. If the SOC is included, spin degeneracy will be lifted therefore all bands are non-degenerate

except either at the high symmetry planes or the quasi-symmetry protected planes [Fig. S4(b)]. This difference is exemplified for the Fermi surface orbits with different field directions. When the magnetic field is applied along [100] axis, the non-SOC orbits are four-fold degenerate [Fig. S4 (c)] while for SOC-included case the orbits are doubly degenerate [Fig. S4 (d)]. In the meantime for $B//[110]$ the non-SOC orbits are doubly degenerate except at the high symmetry lines [Fig. S4 (e)], while for SOC-included case the four orbits are almost singly degenerate [Fig. S4 (f)] yet displays a complex intersecting pattern with degeneracies occur only at certain k-point. The three-dimensional (3D) view of the Fermi surfaces for both non-SOC and SOC-included cases are displayed in Fig. S4 (g) and (h) respectively.

III. NEAR-DEGENERACY DUE TO QUASI-SYMMETRY

To display the near-degeneracy due to quasi-symmetries, Fermi surfaces with different orbital and spin characters, namely $1^+/2^-$ and $1^-/2^+$, are paired up (Fig. S5). The intersections between the Fermi surfaces form four rings for each pair and therefore eight rings in total. As the position of the degenerate rings strongly depend on the size and shape of the Fermi surfaces, by tuning the Fermi level of the system, the degenerate rings are reshaped and relocated in the Brillouin zone (Fig. S6). When the Fermi level is tuned to the type-II Weyl point located along the R to Γ line, the degenerate rings shrink to eight singular Weyl points at the Fermi surface and vanish with further reducing the Fermi level. By combining all degenerate rings at different Fermi energy, degenerate planes protected by the quasi-symmetry is constructed (Fig. S7). The degenerate planes contain eight different planes which are all symmetrically related (Fig. S8).

IV. SHUBNIKOV–DE HAAS OSCILLATION MEASUREMENTS OF COSI

Two microstructure devices are fabricated by focused-ion-beam technique in order to perform Shubnikov–de Haas (SdH) oscillation measurements with field applied along different directions. For Device-1, a microbar along [100] axis with a cross section area of 6 by 6 μm^2 is fabricated [Fig. S9 (a)], and the quantum oscillations are measured with magnetic field rotate within the (100) plane [Fig. S9 (b)]. This ensures the magnetic field direction is always perpendicular to the current direction which eliminates the possible influence of longitudinal magnetotransport. The SdH oscillations are measured with a 10-degree-step rotation starting from [001] axis [Fig. S9

(c)], and the corresponding angle-dependent fast-Fourier-transformation spectrum is displayed in Fig. S9 (d). To further investigate the Fermi surface property, another micro-bar along $[1\bar{1}0]$ axis is fabricated [Fig. S10 (a)]. The magnetic field is therefore rotated from $[001]$ to $[110]$ axis [Fig. S10 (b)]. Angle-dependent SdH oscillations and corresponding FFT spectrum are displayed in Fig. S10 (c) and (d) respectively. The angular dependence of oscillation frequency is summarized in Fig. S10 (e). Similarly, the experimental results match well with the quasi-symmetry scenario while the avoid-crossing prediction failed to explain the experimental results, which further demonstrates the importance of quasi-symmetry in CoSi.

V. CALCULATION OF MAGNETIC BREAKDOWN FIELD

Theoretically, the magnetic breakdown probability is defined as³:

$$P = e^{-H_0/H} \quad (\text{S1})$$

where H_0 is the magnetic breakdown field given by:

$$H_0 = \frac{\pi}{4\hbar e} \frac{\Delta^2}{v_{\parallel}v_{\perp}} \quad (\text{S2})$$

here v_{\parallel} and v_{\perp} stand for the Fermi velocity along two in-plane directions perpendicular to the magnetic field. For example, with field applied along $[110]$ axis, v_{\parallel} is the Fermi velocity along $[001]$ axis while v_{\perp} stands for Fermi velocity along $[1\bar{1}0]$ direction. From band structure calculation we obtained:

$$v_{\parallel} = 2.11 \times 10^5 \text{ m/s}, \quad v_{\perp} = 2.64 \times 10^5 \text{ m/s} \quad (\text{S3})$$

Meanwhile the breakdown gap $\Delta \approx 2$ meV as presented in Fig. S11 (d). Therefore the magnetic breakdown field is estimated to be around 0.11 T. Such a small magnetic breakdown field supports the validity of our quasi-symmetry model. For other field orientations, the breakdown gap remains smaller than 2 meV (Fig. S11) and the corresponding breakdown field H_0 at any arbitrary field direction is always smaller than 0.11 T.

VI. THEORETICAL MODELLING

A. Space group 198 of CoSi

The chiral crystal CoSi has a space group 198 (SG198), which can be generated by

$$S_{2x} = \{C_{2x}|\frac{1}{2}\frac{1}{2}0\}, C_3 = \{C_{3,(111)}|000\}, \quad (\text{S4})$$

in addition to the translation sub-group⁷. Hereafter, the Seitz notation is taken for the non-symmorphic symmetry operations, i.e., a point group operation \mathcal{O} followed by a translation $\mathbf{v} = v_i \mathbf{t}_i$, labeled as $\hat{\mathcal{O}} = \{\mathcal{O}|\mathbf{v}\}$ or $\hat{\mathcal{O}} = \{\mathcal{O}|v_1v_2v_3\}$, with \mathbf{t}_i ($i = 1, 2, 3$) representing three basis vectors for a Bravais lattice in three dimensions [see Fig. 2(a) in the main text] The reciprocal space lattice vectors are generated by \mathbf{g}_i , where $\mathbf{g}_i \cdot \mathbf{t}_j = 2\pi\delta_{ij}$. The rules for multiplication and inversion are defined as

$$\{\mathcal{O}_2|\mathbf{v}_2\}\{\mathcal{O}_1|\mathbf{v}_1\} = \{\mathcal{O}_2\mathcal{O}_1|\mathbf{v}_2 + \mathcal{O}_2\mathbf{v}_1\}, \quad (\text{S5})$$

$$\{\mathcal{O}|\mathbf{v}\}^{-1} = \{\mathcal{O}^{-1}|-\mathcal{O}^{-1}\mathbf{v}\}. \quad (\text{S6})$$

The $S_{2y} = \{C_{2y}|0\frac{1}{2}\frac{1}{2}\}$ symmetry can be generated by

$$S_{2y} = C_3^{-1}S_{2x}C_3, \quad (\text{S7})$$

where we take the convention for $C_{3,(111)} : (x, y, z) \rightarrow (y, z, x)$, leading to $C_{2y} = C_{3,(111)}^{-1}C_{2x}C_{3,(111)}$. Likewise, the S_{2z} symmetry can be given by the combination of S_{2x} , S_{2y} and the translation operator $E_{\mathbf{v}} = \{E|\mathbf{v}\}$,

$$S_{2x}S_{2y} = \{E|00\bar{1}\}S_{2z} \triangleq E_{00\bar{1}}S_{2z}. \quad (\text{S8})$$

Similar to the MnSi in Ref. [5], the symmetry-enforced nodal planes (high symmetry planes) also exist for CoSi. On these high-symmetry planes, the two-fold degeneracies are protected by the combined anti-unitary symmetries, $S_{2x}\mathcal{T}$, $S_{2y}\mathcal{T}$ and $S_{2z}\mathcal{T}$, where \mathcal{T} is the time-reversal operator. For spinless fermions, $\mathcal{T} = \mathcal{K}$ with the complex conjugate \mathcal{K} , while for the spin-1/2 fermions, $\mathcal{T} = is_y\mathcal{K}$ with s_y the Pauli matrix acting on the spin subspace. These operations transform the Hamiltonian as

$$(S_{2x}\mathcal{T})^\dagger \mathcal{H}(k_x, k_y, k_z) (S_{2x}\mathcal{T}) = \mathcal{H}(-k_x, k_y, k_z), \quad (\text{S9})$$

$$(S_{2y}\mathcal{T})^\dagger \mathcal{H}(k_x, k_y, k_z) (S_{2y}\mathcal{T}) = \mathcal{H}(k_x, -k_y, k_z), \quad (\text{S10})$$

$$(S_{2z}\mathcal{T})^\dagger \mathcal{H}(k_x, k_y, k_z) (S_{2z}\mathcal{T}) = \mathcal{H}(k_x, k_y, -k_z). \quad (\text{S11})$$

It indicates that $[S_{2x}\mathcal{T}, \mathcal{H}(k_x = 0, \pi, k_y, k_z)] = 0$ for the $k_x = 0, \pi$ planes. Likewise, the $S_{2y}\mathcal{T}$ -invariant ($S_{2z}\mathcal{T}$ -invariant) planes are $k_y = 0, \pi$ ($k_z = 0, \pi$). Moreover, we act the operators $S_{2x}\mathcal{T}$, $S_{2y}\mathcal{T}$ and $S_{2z}\mathcal{T}$ on the Bloch wave functions at \mathbf{k} and find $(S_{2x}\mathcal{T})^2 = (S_{2y}\mathcal{T})^2 = (S_{2z}\mathcal{T})^2 = -1$ at the $k_i = \pi$ plane. Thus, $S_{2x}\mathcal{T}$, $S_{2y}\mathcal{T}$ and $S_{2z}\mathcal{T}$ behave as the time reversal operator for spinful fermions, and the two-fold degeneracy on the $k_{x,y,z} = \pi$ -plane can be guaranteed by these anti-unitary symmetries, similar to the Kramers' theorem, as depicted in Fig. S4(c).

B. The effective model Hamiltonian around the R -point

In this section, we construct the effective $\mathbf{k} \cdot \mathbf{p}$ Hamiltonian around the R -point ($\mathbf{k}_R = (\pi, \pi, \pi)$), and fit parameters for the $\mathbf{k} \cdot \mathbf{p}$ bands with the density-functional-theory (DFT) bands.

We first consider the commutation relations of the symmetry operators S_{2x} , S_{2y} and \mathcal{T} in SG198 for spinless fermions at R , given by

$$\{S_{2x}, S_{2y}\} = 0, [\mathcal{T}, S_{2x}] = [\mathcal{T}, S_{2y}] = 0 \text{ and } (S_{2x}\mathcal{T})^2 = (S_{2y}\mathcal{T})^2 = -1. \quad (\text{S12})$$

For a common eigen-state $|\Psi\rangle$ of S_{2x} with eigenvalue λ and the Hamiltonian, the S_{2x} -eigenvalues of the states $S_{2y}|\Psi\rangle$, $\mathcal{T}|\Psi\rangle$ and $S_{2y}\mathcal{T}|\Psi\rangle$ are given in the following table,

	$ \Psi\rangle$	$S_{2y} \Psi\rangle$	$\mathcal{T} \Psi\rangle$	$S_{2y}\mathcal{T} \Psi\rangle$
S_{2x}	λ	$-\lambda$	$\lambda^* = -\lambda$	$-\lambda^* = \lambda$

from which we find $|\Psi\rangle, S_{2y}\mathcal{T}|\Psi\rangle$ and $S_{2y}|\Psi\rangle, \mathcal{T}|\Psi\rangle$ carry opposite S_{2x} -eigenvalues. Here we have used the fact that λ is a purely imaginary number due to $S_{2x}^2 = -1$. Furthermore, since $(S_{2y}\mathcal{T})^2 = -1$ and $S_{2y}\mathcal{T}$ is an anti-unitary symmetry operator, $\langle\Psi|S_{2y}\mathcal{T}|\Psi\rangle = 0$, which means the states $|\Psi\rangle$ and $S_{2y}\mathcal{T}|\Psi\rangle$ ($S_{2y}|\Psi\rangle$ and $\mathcal{T}|\Psi\rangle$) are orthogonal to each other. Thus, $\{|\Psi\rangle, S_{2y}|\Psi\rangle, \mathcal{T}|\Psi\rangle, S_{2y}\mathcal{T}|\Psi\rangle\}$ are four independent degenerate eigen-states of the Hamiltonian. This proves all the eigen-states of the Hamiltonian at the R -point are four-fold degenerate (without spin), and thus supports the discussions in the main text above Eq. (1).

Next we will construct the effective model on the four-fold degenerate states based on the symmetry argument. Let us choose G_1, G_2 and G_3 to be the matrix representations for the S_{2x} , S_{2y} , and C_3 , respectively. Without spin, these matrix representations need to satisfy the relations

$$G_3^3 = 1, G_1^2 = G_2^2 = -1, G_1G_2 = -G_2G_1, G_3^{-1}G_1G_3 = G_2, G_3^{-1}G_2G_3 = -G_1G_2. \quad (\text{S13})$$

Moreover, all of them commute with time-reversal symmetry, $[G_1, \mathcal{T}] = [G_2, \mathcal{T}] = [G_3, \mathcal{T}] = 0$ for $\mathcal{T} = K$. Thus, one can construct the 4D irreducible representation matrices for G_1, G_2 and G_3 as

$$G_3 = \begin{pmatrix} 1 & 0 & 0 & 0 \\ 0 & 0 & -1 & 0 \\ 0 & 0 & 0 & 1 \\ 0 & -1 & 0 & 0 \end{pmatrix}, G_1 = \begin{pmatrix} 0 & 0 & 1 & 0 \\ 0 & 0 & 0 & 1 \\ -1 & 0 & 0 & 0 \\ 0 & -1 & 0 & 0 \end{pmatrix} = i\sigma_y\tau_0, G_2 = \begin{pmatrix} 0 & 0 & 0 & 1 \\ 0 & 0 & -1 & 0 \\ 0 & 1 & 0 & 0 \\ -1 & 0 & 0 & 0 \end{pmatrix} = i\sigma_x\tau_y. \quad (\text{S14})$$

Here we have chosen two sets of Pauli matrices σ and τ to rewrite the four by four matrices.

Based on the above three transformation matrices for G_1, G_2 and G_3 and time reversal operator $\mathcal{T} = \mathcal{K}$, we can construct the effective Hamiltonian around the R-point as (without spin)

$$\mathcal{H}_{non-soc}(\mathbf{k}) = \mathcal{H}_0(\mathbf{k}) + \mathcal{H}_{k^2}(\mathbf{k}), \quad (\text{S15})$$

where the the leading order Hamiltonian reads

$$\mathcal{H}_0(\mathbf{k}) = C_0\sigma_0\tau_0 + A_1(k_x\sigma_y\tau_0 + k_y\sigma_x\tau_y - k_z\sigma_z\tau_y), \quad (\text{S16})$$

and the k^2 -order Hamiltonian is

$$\begin{aligned} \mathcal{H}_{k^2}(\mathbf{k}) = & B_1k^2\sigma_0\tau_0 + C_1(k_xk_y\sigma_z\tau_0 + k_yk_z\sigma_0\tau_z + k_xk_z\sigma_z\tau_z) + C_2(k_xk_y\sigma_x\tau_x \\ & - k_yk_z\sigma_0\tau_x + k_xk_z\sigma_x\tau_0) + C_3(k_xk_y\sigma_x\tau_z - k_yk_z\sigma_y\tau_y - k_xk_z\sigma_z\tau_x), \end{aligned} \quad (\text{S17})$$

with $C_0, A_1, B_1, C_1, C_2, C_3$ material-dependent parameters and $k = \sqrt{k_x^2 + k_y^2 + k_z^2}$.

Next we will include spin-orbit coupling into the Hamiltonian. To do that, we note that spin is a pseudo-vector and behaves exactly the same as a vector due to the lack of inversion, mirror or other roto-inversion symmetries for a chiral crystal. Correspondingly, we just need to replace the momentum \mathbf{k} by the Pauli matrices \mathbf{s} of the electron spin to get the effective spin-orbit coupling, which is written as

$$\mathcal{H}_{soc} = \lambda_0(s_x\sigma_y\tau_0 + s_y\sigma_x\tau_y - s_z\sigma_z\tau_y), \quad (\text{S18})$$

up to the first order in spin, with the spin-orbit coupling parameter λ_0 . The full Hamiltonian is given by

$$\mathcal{H}_R(\mathbf{k}) = \mathcal{H}_{non-soc} \otimes s_0 + \mathcal{H}_{soc}. \quad (\text{S19})$$

For $\lambda_0 = 0$, one can check that the Hamiltonian $\mathcal{H}_R(\mathbf{k})$ has a 8-fold degeneracy at R -point ($\mathbf{k} = 0$). Once the spin-orbit coupling is turned on, the 8-fold degeneracy at R -point is split into a 6-fold (energy λ_0) and a 2-fold (energy $-3\lambda_0$). From the DFT calculation [see Fig. 2(c) in the main text], we find that the 6-fold degenerated states have higher energy than that of the 2-fold states, which implies $\lambda_0 > 0$.

The spin-independent Hamiltonian $\mathcal{H}_0(\mathbf{k})$ is isotropic with the full rotation symmetry. To see that, we could define the emergent angular momentum operators as

$$L_x = \frac{1}{2}\sigma_y\tau_0, \quad L_y = \frac{1}{2}\sigma_x\tau_y, \quad L_z = -\frac{1}{2}\sigma_z\tau_y, \quad (\text{S20})$$

which satisfies the commutation relation $[L_i, L_j] = i\epsilon_{ijk}L_k$ with Levi-Civita symbol ϵ_{ijk} and $i = x, y, z$. Therefore, $\mathcal{H}_0(\mathbf{k})$ and \mathcal{H}_{soc} can be re-written as

$$\mathcal{H}_0(\mathbf{k}) = C_0\sigma_0\tau_0 + 2A_1(\mathbf{k} \cdot \mathbf{L}), \quad (\text{S21})$$

$$\mathcal{H}_{soc} = 2\lambda_0(\mathbf{s} \cdot \mathbf{L}), \quad (\text{S22})$$

which is shown in the Eq. (1) in the main text. $\mathcal{H}_{k^2}(\mathbf{k})$ breaks the full rotational symmetry. Moreover, we extract the parameters for the R -model in Eq. (S19) by fitting the DFT bands along high symmetry lines, shown in Fig. S12. The parameters are

$$\begin{aligned} C_0 &= -0.18 \text{ eV}, \lambda_0 = 0.0075 \text{ eV}, B_1 = 2.123 \text{ eV} \cdot \text{\AA}^2, A_1 = 0.853 \text{ eV} \cdot \text{\AA}, \\ C_1 &= -0.042 \text{ eV} \cdot \text{\AA}^2, C_2 = 0.546 \text{ eV} \cdot \text{\AA}^2, C_3 = 3.345 \text{ eV} \cdot \text{\AA}^2. \end{aligned} \quad (\text{S23})$$

With this set of parameters, the bands near the R -point from the DFT are well reproduced by the effective model, shown in Fig. S12 (b).

C. The perturbation theory around the Fermi energy

According to the DFT calculation as well as the results from the effective R model in Eq. (S19), we find the near crossings which are consistent with the experimental results. A tiny gap (~ 1 meV) for the near crossings is shown in Fig. S13 (a). To understand the origin of this tiny gap, we apply the perturbation theory to the model Hamiltonian (S19). We treat $\mathcal{H}_0(\mathbf{k}) \otimes s_0$ as the unperturbed Hamiltonian and $\mathcal{H}_{perb} = \mathcal{H}_{soc} + \mathcal{H}_{k^2}(\mathbf{k})$ as the perturbation Hamiltonian.

We first solve the eigen-problem of the Hamiltonian $\mathcal{H}_0(\mathbf{k}) \otimes s_0$ and due to its full rotation symmetry, we choose the spherical coordinate for the momentum $\mathbf{k} = (k_x, k_y, k_z) =$

$k(\sin \theta \cos \phi, \sin \theta \sin \phi, \cos \theta)$. The eigen-energies of $\mathcal{H}_0(\mathbf{k}) \otimes s_0$ have two branches $E_{\pm} = C_0 \pm A_1 k$ for which each branch has four-fold degeneracy. The four degenerate eigen-wave functions of the positive energy branch (E_+) are given by

$$\begin{aligned} |\Psi_{A+\uparrow}(\theta, \phi)\rangle &= |\Psi_{A+}(\theta, \phi)\rangle \otimes (1, 0)^T, \\ |\Psi_{B+\uparrow}(\theta, \phi)\rangle &= |\Psi_{B+}(\theta, \phi)\rangle \otimes (1, 0)^T, \\ |\Psi_{A+\downarrow}(\theta, \phi)\rangle &= |\Psi_{A+}(\theta, \phi)\rangle \otimes (0, 1)^T, \\ |\Psi_{B+\downarrow}(\theta, \phi)\rangle &= |\Psi_{B+}(\theta, \phi)\rangle \otimes (0, 1)^T, \end{aligned} \quad (\text{S24})$$

where the spin-independent components are

$$|\Psi_{A+}(\theta, \phi)\rangle = \frac{1}{\sqrt{2}} (\cos \theta \cos \phi - i \sin \phi, -\cos \theta \sin \phi - i \cos \phi, 0, \sin \theta)^T, \quad (\text{S25})$$

$$|\Psi_{B+}(\theta, \phi)\rangle = \frac{1}{\sqrt{2}} (-i \sin \theta \cos \phi, i \sin \theta \sin \phi, 1, i \cos \theta)^T, \quad (\text{S26})$$

here we use $\{A+, B+\}$ to label the two bands and $\{\uparrow, \downarrow\}$ for the electron spin.

Then, we can project the angular momentum operator \mathbf{L} into the eigenstate subspace and find

$$\langle \Psi_{A+}(\theta, \phi) | \mathbf{L} | \Psi_{A+}(\theta, \phi) \rangle = \langle \Psi_{B+}(\theta, \phi) | \mathbf{L} | \Psi_{B+}(\theta, \phi) \rangle = \frac{\mathbf{k}}{2k}, \quad (\text{S27})$$

$$\langle \Psi_{A+}(\theta, \phi) | \mathbf{L} | \Psi_{B+}(\theta, \phi) \rangle = \langle \Psi_{B+}(\theta, \phi) | \mathbf{L} | \Psi_{A+}(\theta, \phi) \rangle = 0, \quad (\text{S28})$$

which means the emergent angular momentum operator \mathbf{L} is projected into the momentum direction. Thus up to the first-order perturbation, the spin-orbit coupling term becomes the form of $\frac{\lambda_0}{k} (\mathbf{k} \cdot \mathbf{s}) \otimes I_{2 \times 2}$ after projecting into the eigen-state subspace,

$$|\Psi_{upper}\rangle = \{|\Psi_{A+\uparrow}(\theta, \phi)\rangle, |\Psi_{B+\uparrow}(\theta, \phi)\rangle, |\Psi_{A+\downarrow}(\theta, \phi)\rangle, |\Psi_{B+\downarrow}(\theta, \phi)\rangle\}, \quad (\text{S29})$$

which supports the discussions below Eq. (1) in the main text. The identity matrix $I_{2 \times 2}$ indicates that the first-order perturbation Hamiltonian of SOC does not couple different bands.

Next, we can apply the perturbation theory to consider the perturbation Hamiltonian \mathcal{H}_{perb} in the subspace $|\Psi_{upper}\rangle$ order by order. Up to the first-order perturbation, the perturbed Hamiltonian $\mathcal{H}_P^{eff(1)}$ reads

$$\begin{aligned} \mathcal{H}_P^{eff(1)} &= (C_0 + B_1 k^2 + A_1 k) s_0 \omega_0 + \lambda_0 (\lambda_x s_x + \lambda_y s_y + \lambda_z s_z) \omega_0 \\ &+ \tilde{C} k^2 s_0 (d_x \omega_x + d_y \omega_y + d_z \omega_z). \end{aligned} \quad (\text{S30})$$

where $\tilde{C} = C_1 - C_2 + C_3$, and $\omega_{x,y,z}$ are Pauli matrices for the $\{A+, B+\}$ band subspace [$+$ means the upper four bands in Eq. (S24)]. The coefficient $\lambda_{x,y,z}$ are defined as

$$(\lambda_x, \lambda_y, \lambda_z) = (\sin \theta \cos \phi, \sin \theta \sin \phi, \cos \theta) = \frac{\mathbf{k}}{|\mathbf{k}|}, \quad (\text{S31})$$

and $d_{x,y,z}$ are given by

$$\begin{aligned} d_x &= \cos \theta \sin^2 \theta \sin \phi \cos \phi (\cos \phi + \sin \phi), \\ d_y &= \cos \theta \sin^2 \theta \sin \phi \cos \phi (\sin \theta + \cos \theta (\cos \phi - \sin \phi)), \\ d_z &= \sin^2 \theta \sin \phi \cos \phi (\cos^2 \theta + \sin \theta \cos \theta (-\cos \phi + \sin \phi)). \end{aligned} \quad (\text{S32})$$

The perturbation theory is valid only for $A_1 k \gg \lambda_0$ and $A_1 k \gg \frac{\sqrt{3}}{4} \tilde{C} k^2$. With the parameters used in this work [see Eq. (S23)], we can estimate the valid range of the momentum as

$$k_{min} < k < k_{max} \quad \Leftarrow \quad k_{min} = \frac{\lambda_0}{A_1} \approx 0.01 \text{ \AA}^{-1} \text{ and } k_{max} = \frac{4A_1}{\sqrt{3}\tilde{C}} \approx 0.7 \text{ \AA}^{-1}. \quad (\text{S33})$$

The eigen-energies of the effective Hamiltonian (S30) are given by

$$E_{\alpha\beta}(k, \theta, \phi) = C_0 + B_1 k^2 + A_1 k + \alpha \lambda_0 + \beta \frac{\sqrt{3}}{4} \tilde{C} k^2 |\sin 2\phi \sin 2\theta \sin \theta|, \quad (\text{S34})$$

where $\alpha = \pm$ and $\beta = \pm$. These energy dispersions show the exact crossings in Fig. S13(b). Note that $\sin 2\phi \sin 2\theta \sin \theta = 4k_x k_y k_z / k^3$, indicating the perturbation correction of \mathcal{H}_{k^2} breaks the full rotational symmetry down to three-fold rotational symmetry.

Next we consider the second-order perturbation corrections, which open a tiny gap for the emergent nodal lines [see Fig. S13(c)]. For the second-order perturbation, besides the eigen-state basis set $|\Psi_{upper}\rangle$ in Eq. (S24), we also need to take four negative energy (E_-) eigen-states

$$|\Psi_{lower}\rangle = \{|\Psi_{A-\uparrow}(\theta, \phi)\rangle, |\Psi_{B-\uparrow}(\theta, \phi)\rangle, |\Psi_{A-\downarrow}(\theta, \phi)\rangle, |\Psi_{B-\downarrow}(\theta, \phi)\rangle\}, \quad (\text{S35})$$

with the explicit expressions

$$\begin{aligned} |\Psi_{A-\uparrow}(\theta, \phi)\rangle &= \frac{1}{\sqrt{2}} (\cos \theta \cos \phi + i \sin \phi, -\cos \theta \sin \phi + i \cos \phi, 0, \sin \theta, 0, 0, 0, 0)^T, \\ |\Psi_{B-\uparrow}(\theta, \phi)\rangle &= \frac{1}{\sqrt{2}} (i \sin \theta \cos \phi, -i \sin \theta \sin \phi, 1, -i \cos \theta, 0, 0, 0, 0), \\ |\Psi_{A-\downarrow}(\theta, \phi)\rangle &= \frac{1}{\sqrt{2}} (0, 0, 0, 0, \cos \theta \cos \phi + i \sin \phi, -\cos \theta \sin \phi + i \cos \phi, 0, \sin \theta)^T, \\ |\Psi_{B-\downarrow}(\theta, \phi)\rangle &= \frac{1}{\sqrt{2}} (0, 0, 0, 0, i \sin \theta \cos \phi, -i \sin \theta \sin \phi, 1, -i \cos \theta). \end{aligned} \quad (\text{S36})$$

The second-order perturbed Hamiltonian is given by

$$\Delta \mathcal{H}_P^{eff(2)} = \frac{1}{\Delta E} \left(\langle \Psi_{upper} | (\mathcal{H}_{soc} + \mathcal{H}_{k^2}(\mathbf{k})) \hat{P}_{lower} (\mathcal{H}_{soc} + \mathcal{H}_{k^2}(\mathbf{k})) | \Psi_{upper} \rangle \right), \quad (\text{S37})$$

where $\Delta E = E_+ - E_- = 2A_1 k$ is the energy difference and the projection operator $\hat{P}_{lower} = |\Psi_{lower}\rangle \langle \Psi_{lower}|$ onto the lower four bands in Eq. (S35). To simplify the problem, we only consider the mixed terms of \mathcal{H}_{soc} and $\mathcal{H}_{k^2}(\mathbf{k})$, given by

$$\Delta \mathcal{H}_P^{eff(2)} = \frac{1}{\Delta E} (\langle \Psi_{upper} | \mathcal{H}_{soc} | \Psi_{lower} \rangle \langle \Psi_{lower} | \mathcal{H}_{k^2}(\mathbf{k}) | \Psi_{upper} \rangle) + \text{h.c.}, \quad (\text{S38})$$

The matrix elements of $\Delta\mathcal{H}_P^{eff(2)}$ are,

$$\left[\Delta\mathcal{H}_P^{eff(2)}\right]_{1,1} = 2 \sin^2(\theta) \sin(\phi) \cos(\phi) \left(\sin^3(\theta) \sin(\phi) + \sin(\theta) \cos^2(\theta) \cos(\phi) - \cos^3(\theta) \right), \quad (\text{S39})$$

$$\left[\Delta\mathcal{H}_P^{eff(2)}\right]_{1,2} = \sin^2(\theta) \cos(\phi) (\sin^2(\theta) \sin(2\phi) + 2i \cos(\theta) \sin(\phi) (\cos(\theta) (\cos(\theta) \cos(\phi) + \sin(\theta)) + \sin(\phi) (\sin^2(\theta) + i \cos(\theta))))), \quad (\text{S40})$$

$$\left[\Delta\mathcal{H}_P^{eff(2)}\right]_{1,3} = \frac{1}{4} e^{-i\phi} \sin(\theta) \cos(\theta) (\sin(2\phi) (\sin(3\theta) \sin(\phi) + 4 \cos^3(\theta)) - 8 \sin(\theta) \cos^2(\theta) \sin(\phi) \cos^2(\phi) + 8i \cos(\theta) \sin^2(\phi) + (-\frac{3}{2} + 6i) \sin(\theta) \cos(\phi) + (\frac{3}{2} + 2i) \sin(\theta) \cos(3\phi)), \quad (\text{S41})$$

$$\left[\Delta\mathcal{H}_P^{eff(2)}\right]_{1,4} = e^{-i\phi} \sin(\theta) ((\cos(\theta) - 1) (\cos^2(\theta) \cos(\phi) + i \sin(\theta) \sin(\phi) \cos(\phi) (-\cos^2(\theta) + \sin(\theta) (\cos(\theta) + i) \cos(\phi)) + \sin(\theta) \cos(\theta) \sin^2(\phi) (-1 - i \sin(\theta) \cos(\phi))) - 2i \cos^2(\frac{\theta}{2}) (-i \cos^2(\theta) \cos(\phi) \cos(2\phi) + \sin(\phi) \cos(\phi) ((\cos^3(\theta) + \cos(\theta)) \cos(\phi) - i \sin^2(\theta) \cos(\phi) + \sin(\theta) \cos^2(\theta)) + \sin(\theta) \cos(\theta) \sin^2(\phi) (\sin(\theta) \cos(\phi) + i))) \quad (\text{S42})$$

and

$$\left[\Delta\mathcal{H}_P^{eff(2)}\right]_{2,2} = -\frac{1}{4} \sin^5(\theta) \sin(\phi) \sin(2\phi) \left(\cot^2(\theta) (-4 \cot(\theta) \csc(\phi) + 4 \cot(\phi) - 1) + \csc^2(\theta) + 3 \right), \quad (\text{S43})$$

$$\left[\Delta\mathcal{H}_P^{eff(2)}\right]_{2,3} = \frac{1}{2} e^{-i\phi} \sin(\theta) \cos(\theta) \left(-4 \sin(\phi) (\sin(\theta) \sin(\phi) + (2 + 2i) \sin^2(\frac{\theta}{2}) \cos^2(\phi)) + \cos^2(\theta) \sin(2\phi) (-4i \sin^2(\frac{\theta}{2}) \cos(\phi) + 2i \sin(\theta) + \csc(\phi)) + \cos(\theta) \csc(\phi) (- (2 + 2i) \sin^2(\frac{\theta}{2}) \sin^2(2\phi) + \sin^2(\frac{\theta}{2}) \sin(4\phi) + 4i \sin^2(\theta) \sin^3(\phi) \cos(\phi) + \sin(2\phi)) \right), \quad (\text{S44})$$

$$\left[\Delta\mathcal{H}_P^{eff(2)}\right]_{2,4} = -\frac{1}{8} e^{-i\phi} \sin(\theta) \cos(\theta) (8 \cos^3(\theta) \sin(2\phi) - 16 \sin(\theta) \cos^2(\theta) \sin(\phi) \cos^2(\phi) + 16i \cos(\theta) \sin^2(\phi) + \cos(\phi) (4 \sin(3\theta) \sin^2(\phi) + (-3 + 12i) \sin(\theta)) + (3 + 4i) \sin(\theta) \cos(3\phi)), \quad (\text{S45})$$

and

$$\begin{aligned} \left[\Delta \mathcal{H}_P^{eff(2)} \right]_{3,3} &= -\frac{1}{4} \sin^5(\theta) \sin(\phi) \sin(2\phi) \\ &\quad (\cot^2(\theta)(-4 \cot(\theta) \csc(\phi) + 4 \cot(\phi) - 1) + \csc^2(\theta) + 3), \end{aligned} \quad (\text{S46})$$

$$\begin{aligned} \left[\Delta \mathcal{H}_P^{eff(2)} \right]_{3,4} &= -i \sin^2(\theta) \sin(\phi) \cos(\phi) (2 \cos^3(\theta) \cos(\phi) + 2 \cos^2(\theta) (\sin(\theta) + i \sin(\phi))) \\ &\quad + \sin(\theta) (\sin(2\theta) \sin(\phi) - 2i \sin(\theta) \cos(\phi)), \end{aligned} \quad (\text{S47})$$

and

$$\left[\Delta \mathcal{H}_P^{eff(2)} \right]_{4,4} = 2 \sin^2(\theta) \sin(\phi) \cos(\phi) (\sin^3(\theta) \sin(\phi) + \sin(\theta) \cos^2(\theta) \cos(\phi) - \cos^3(\theta)), \quad (\text{S48})$$

And the other parts are related by conjugation $\left[\Delta \mathcal{H}_P^{eff(2)} \right]_{i,j} = \left[\Delta \mathcal{H}_P^{eff(2)} \right]_{j,i}^*$. The second-order perturbation corrections provides the spin-flipping terms in the effective model and thus generates a tiny gap for the emergent nodal lines on the Fermi surfaces, as shown in Fig. S13 (c).

To simplify the above discussion, we can further project the above four-band P model to the effective model that only consists of the two bands forming the nodal plane. To do that, we consider the eigen-states of the model Hamiltonian (S30) and consider two eigen-states $\{|\alpha = +, \beta = -\rangle, |\alpha = -, \beta = +\rangle\}$ that give the eigen-energies $E_{\alpha=+, \beta=-}$ and $E_{\alpha=-, \beta=+}$ in Eq. S34. Within these two eigen-states, the effective Hamiltonian $\mathcal{H}_P^{eff(1)}$ can be reduced to

$$\mathcal{H}_{eff} = \epsilon_0 + d_z(\mathbf{k}) \sigma_z, \quad (\text{S49})$$

where $\epsilon_0 = C_0 + B_1 k^2 + A_1 k$ and $d_z(\mathbf{k}) = \lambda_0 - \frac{\sqrt{3}}{4} \tilde{C} k^2 |\sin 2\phi \sin 2\theta \sin \theta| = \lambda_0 - \sqrt{3} \tilde{C} \frac{|k_x k_y k_z|}{k}$. This Hamiltonian is the exactly two-band model discussed in the main text. Due to the SOC with $\mathbf{k} \cdot \mathbf{s}$ in the P -model (S34), the spin texture is hexagonal on each Fermi surfaces ($\langle \mathbf{s} \rangle \sim \alpha \mathbf{k}$ with $\alpha = \pm$). Moreover, we plot the spin texture on $E_{\alpha=+, \beta=-}(k, \theta, \phi) = \epsilon_0 + d_z(\mathbf{k}) = E_f$ in Fig. S14 (a), and that for $E_{\alpha=-, \beta=+}(k, \theta, \phi) = \epsilon_0 - d_z(\mathbf{k}) = E_f$ in Fig. S14 (b). It indicates that the crossings between these two Fermi surfaces have opposite spin-polarization. Therefore, according to the low-energy effective Hamiltonian, we can conclude that the spin-conservation plays the role of the quasi-symmetry.

Now we discuss the breaking of the quasi-symmetry by second-order perturbation corrections. To see that, we can further project $\mathcal{H}_P^{eff(2)}$ into the subspace of $\{|\alpha = +, \beta = -\rangle, |\alpha = -, \beta =$

$+\rangle\}$ and the effective Hamiltonian will include two more terms as

$$\mathcal{H}_{eff(2)} = \delta d_x(\mathbf{k})\sigma_x + \delta d_y(\mathbf{k})\sigma_y, \quad (\text{S50})$$

which are due to the spin-flipping terms, breaking the quasi-symmetry. As a result, the co-dimension of the nodal plane becomes 3 instead of 1, explaining the gap opening. While the detailed expressions for δd_x and δd_y are complex, we give an estimate of the typical magnitude of the gap $\Delta_{eff(2)} = 2\sqrt{(\delta d_x)^2 + (\delta d_y)^2} \sim 0.8$ meV for $k_F = 0.13 \text{ \AA}^{-1}$, being the same order with the DFT estimations [see FIG. S11]. By solving $d_z(\mathbf{k}) = 0$ in Eq. (S49), we can find the nodal line on the $\Gamma - R - M$ plane ($\phi = \pi/4$) that is shown in Fig. S14 (c). Furthermore, we calculate the energy gap ($\sqrt{(\delta d_x(\mathbf{k}))^2 + (\delta d_y(\mathbf{k}))^2}$) for the nodal line on the $\Gamma - R - M$ plane, shown in Fig. S14 (d). Please note that the gap vanishes for the type-II Weyl point which locates at $\theta = \arcsin(\sqrt{2/3}) \sim 0.96$ (along the $\Gamma - R$ line), due to the C_3 protection (the two Weyl states have different C_3 -eigenvalues).

D. The Berry curvature distributions

In this section, we show the topologically physical consequence for the emergent nodal lines (near crossing), characterized by the Berry curvature distributions in the momentum space. We calculate the Berry curvature based on the R -model in the $\Gamma - R - M$ plane. Here, we take a standard formula to compute the gauge-invariant Berry curvature

$$\Omega_n(\mathbf{k}) = -\text{Im} \sum_{m \neq n} \frac{\langle n | \nabla \mathcal{H}_R(\mathbf{k}) | m \rangle \times \langle m | \nabla \mathcal{H}_R(\mathbf{k}) | n \rangle}{(E_m - E_n)^2}, \quad (\text{S51})$$

where the velocity operators are given by $\hat{\mathbf{V}} = \nabla \mathcal{H}_R(\mathbf{k}) \triangleq (\hat{V}_x, \hat{V}_y, \hat{V}_z)$. Similar to the analysis in Re. [5] (see Eq. (37) in the Supplementary Materials for the Nature paper of MnSi), we find that

$$S_{2x}\mathcal{T} : (k_x, k_y, k_z) \rightarrow (-k_x, k_y, k_z) \text{ and } \boldsymbol{\Omega}(k_x, k_y, k_z) = \boldsymbol{\Omega}(-k_x, k_y, k_z) \begin{pmatrix} -1 & 0 & 0 \\ 0 & +1 & 0 \\ 0 & 0 & +1 \end{pmatrix}, \quad (\text{S52})$$

$$S_{2y}\mathcal{T} : (k_x, k_y, k_z) \rightarrow (k_x, -k_y, k_z) \text{ and } \boldsymbol{\Omega}(k_x, k_y, k_z) = \boldsymbol{\Omega}(k_x, -k_y, k_z) \begin{pmatrix} +1 & 0 & 0 \\ 0 & -1 & 0 \\ 0 & 0 & +1 \end{pmatrix}, \quad (\text{S53})$$

$$S_{2z}\mathcal{T} : (k_x, k_y, k_z) \rightarrow (k_x, k_y, -k_z) \text{ and } \boldsymbol{\Omega}(k_x, k_y, k_z) = \boldsymbol{\Omega}(k_x, k_y, -k_z) \begin{pmatrix} +1 & 0 & 0 \\ 0 & +1 & 0 \\ 0 & 0 & -1 \end{pmatrix}, \quad (\text{S54})$$

where we take the vector for Berry curvature as $\boldsymbol{\Omega}_n(k_x, k_y, k_z) = (\Omega_{n,yz}, \Omega_{n,zx}, \Omega_{n,xy})$ for the n -th band. The calculated results are shown in Fig. S15 on the $\Gamma - R - M$ plane, confirming the above symmetry requirements. Here we present the Berry curvature for the 1^- -band (see the band notation in Fig. 2 (d) in the main text). Namely, this band is just the second upper-band from the $\mathbf{k} \cdot \mathbf{p}$ -bands, shown in Fig. S12 (c). The three components are shown in Fig. S15 (a),(b) and (c), where the four Fermi surfaces are shown with $E_f = -0.06$ eV. Moreover, the Berry curvature distribution coincides with the emergent nodal lines, illustrated in Fig. S15 (d),(e) and (f). At the R -point or Weyl points, the $U(1)$ Berry curvature is not well defined due to degeneracy, which corresponds to the singularity. In Fig. S15 (a), (b) and (c), the singularity at the R -points is due to the 6-fold degeneracy. And the type-II Weyl points are shown in Fig. S15 (d) for the singularity (marked by the dark-red solid circle).

¹ Koepernik, K., and Eschrig, H., Full-potential nonorthogonal local-orbital minimum-basis band-structure scheme. Phys. Rev. B **59**, 1743 (1999).

- ² Perdew, J. P., Burke, K., and Ernzerhof, M., Generalized gradient approximation made simple. *Phys. Rev. Lett.* **77**, 3865 (1996).
- ³ Blount, E. I., Bloch Electrons in a Magnetic Field. *Phys. Rev.* **126**, 1636 (1962).
- ⁴ Bradlyn, B., Cano, J., Wang, Z., Vergniory, M. G., Felser, C., Cava, R. J., and Bernevig, B. A., Beyond Dirac and Weyl fermions: Unconventional quasiparticles in conventional crystals. *Science* **353**, aaf5037 (2016).
- ⁵ Wilde, M. A., Doderhöft, M., Niedermayr, A., Bauer, A., Hirschmann, M. M., and Alpin, K. et al., Symmetry-enforced topological nodal planes at the Fermi surface of a chiral magnet. *Nature* **594**, 374 (2021).

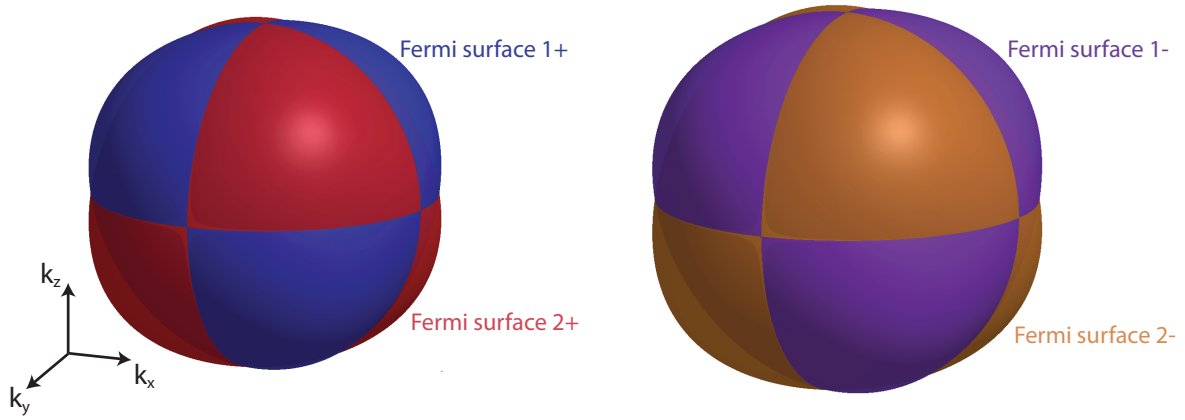


FIG. S1. Fermi surface identification. Two pairs of Fermi surfaces are presented and labelled with their band characters, consistent with the identification in band structure calculations.

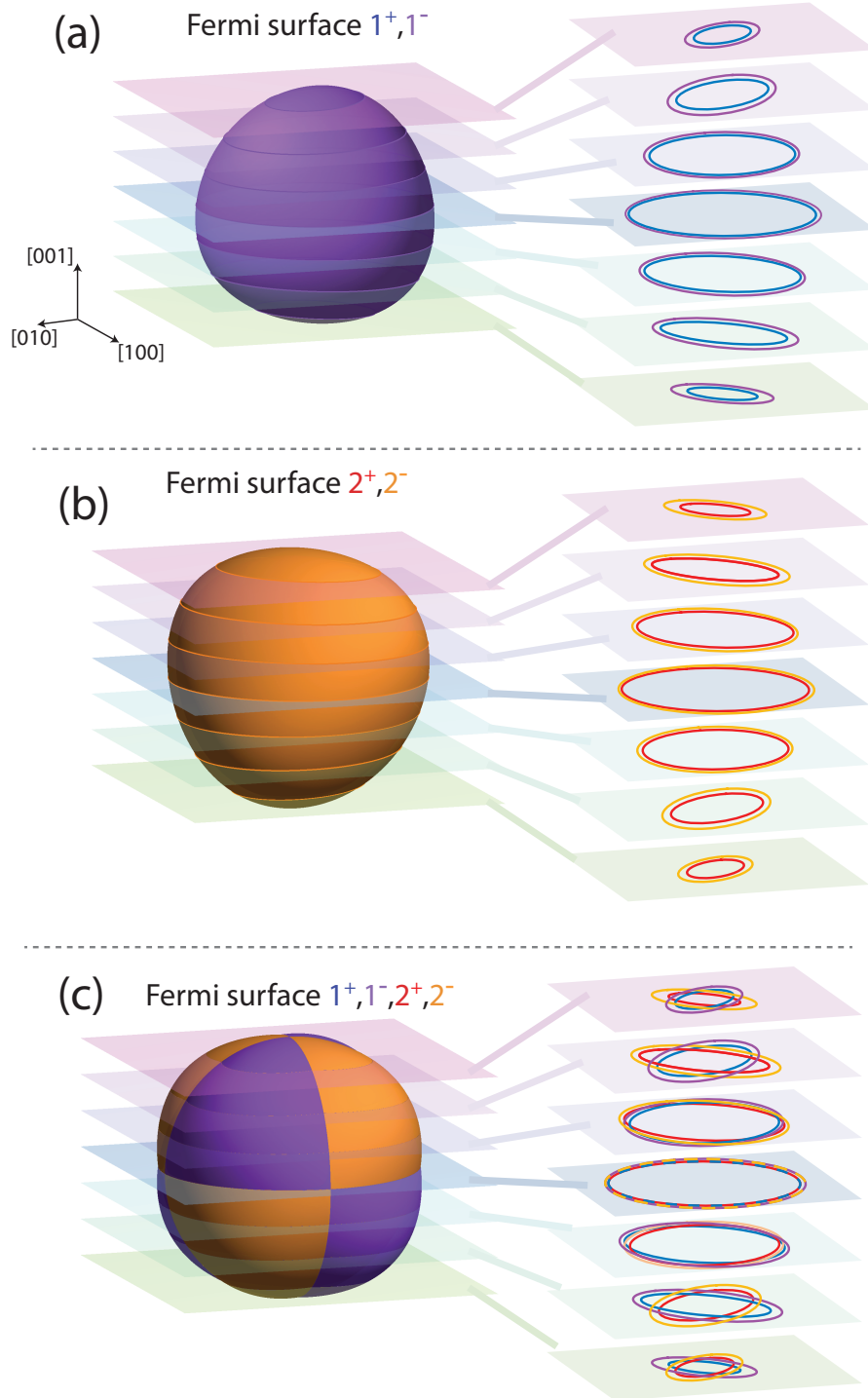


FIG. S2. (a) and (b) present the slice-and-view of Fermi surfaces 1^\pm and 2^\pm respectively. As one can clearly see the sliced orbits of 1^- or 2^- are always larger than 1^+ or 2^+ at any level. This difference is due to spin splitting caused by spin-orbital coupling (SOC). (c) The summarized view of all four Fermi surfaces. It displays four orbits intersect with each other in a complex pattern which results in the degenerate points protected by either crystalline symmetry or quasi-symmetry.

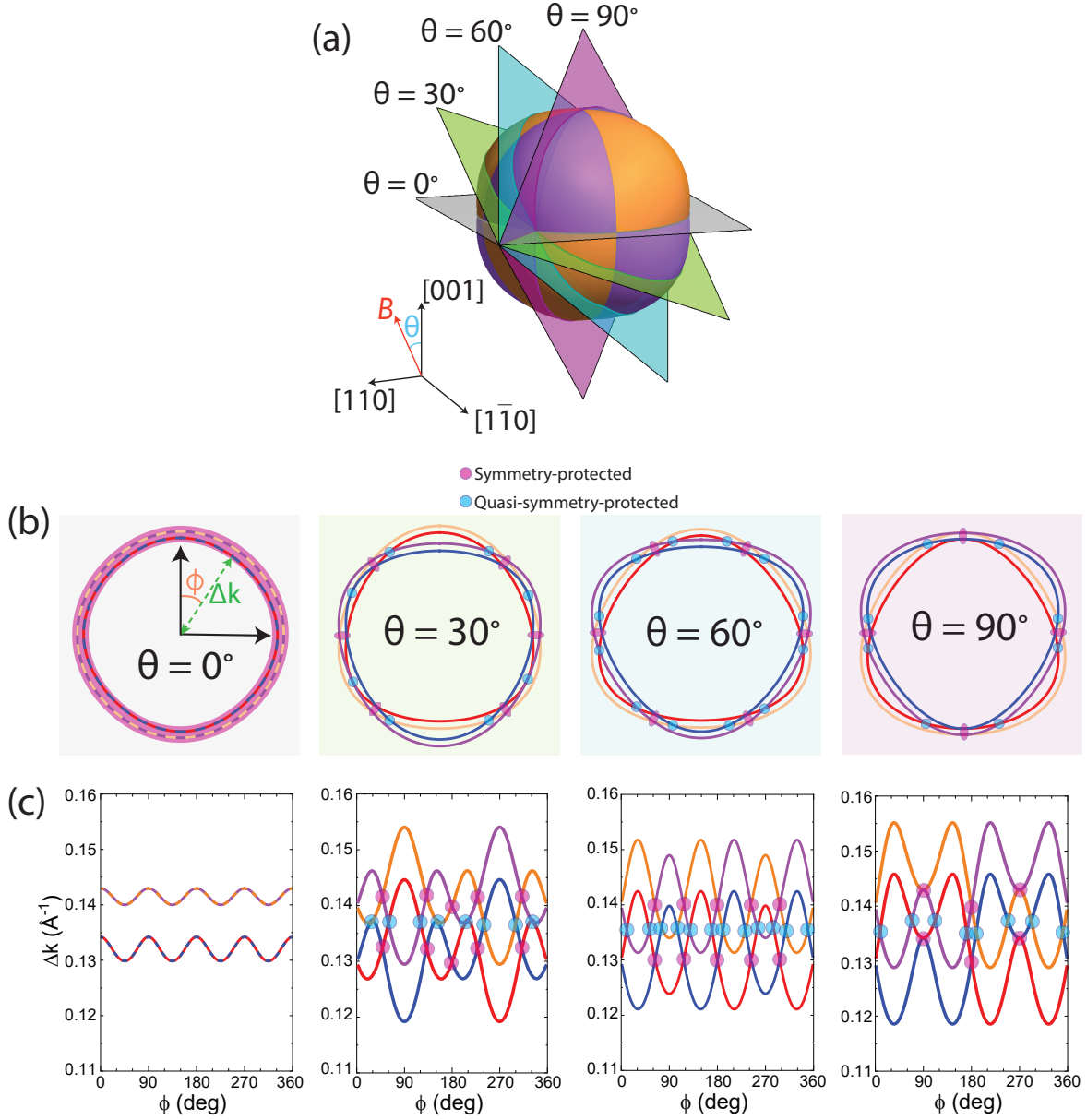


FIG. S3. (a) Illustration of the rotation of magnetic field and the corresponding extremal cross section of Fermi surfaces. Here θ is defined as the angle between field direction and $[001]$ direction, while the square planes stand for the planes perpendicular to the magnetic field. (b) Angle-dependent Fermi surface orbits. The crystalline symmetry and quasi-symmetry protected degeneracies are denoted with pink and blue circles respectively. (c) Momentum difference from R-point Δk as a function of ϕ , which is defined in (b), different types of degenerate points are colored following the color-code in (b).

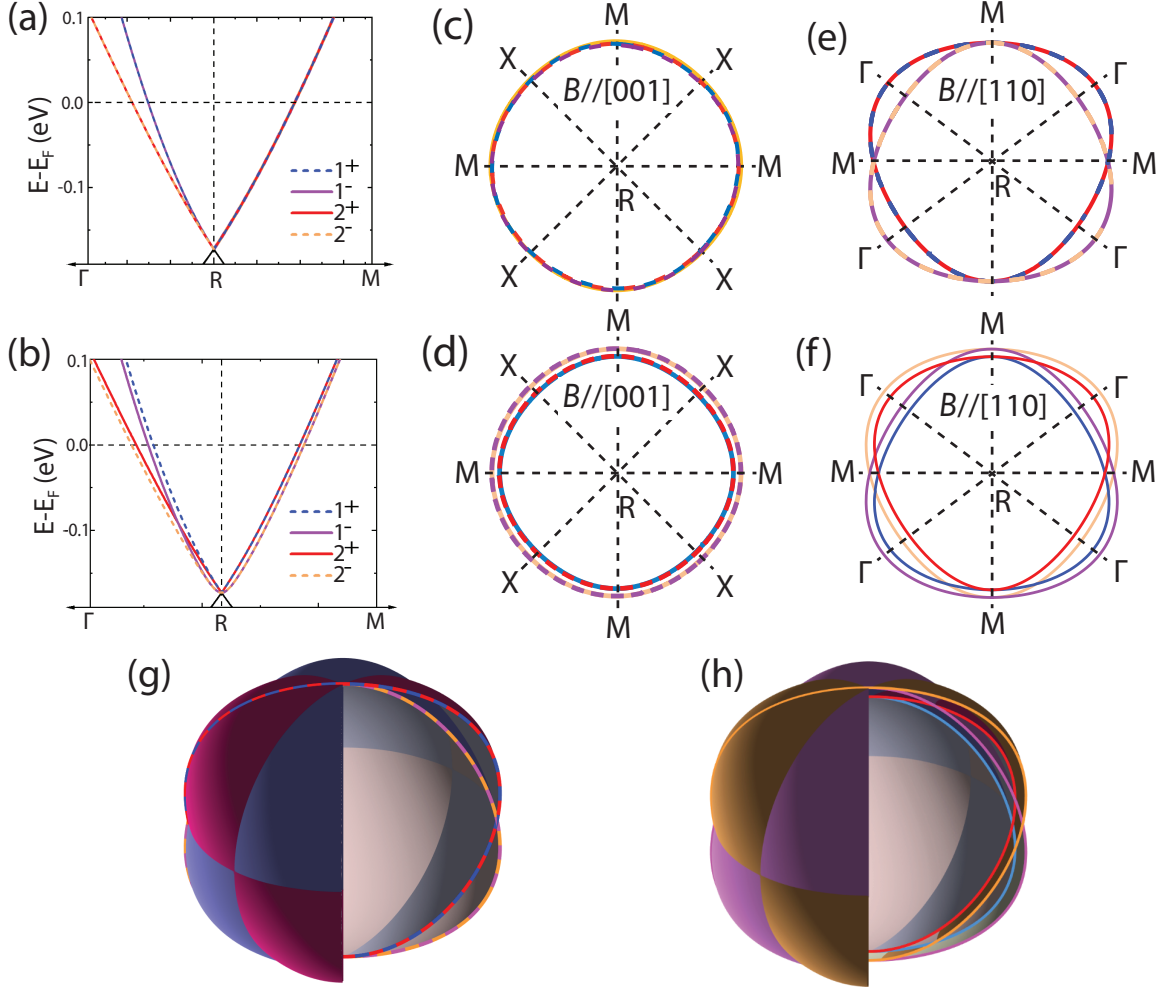
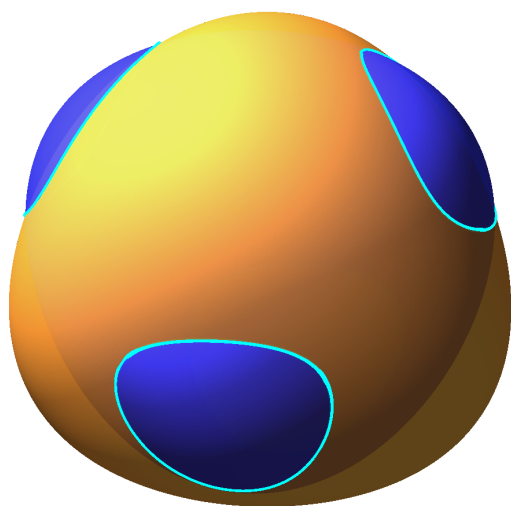


FIG. S4. (a) and (b) display the results of ab-initio band structure calculation around R-point without and with SOC respectively. When SOC is neglected, spin degeneracy is preserved and therefore all bands are at least two-fold degenerate. At the Brillouin zone boundary (i. e. R to M) all four bands are degenerate due to the protection of crystalline symmetry. Taking SOC into account, the spin degeneracy is therefore lifted and only at the Brillouin zone boundary the bands are fully two fold degenerate due to orbital degree of freedom. This spin splitting effect is also clearly demonstrated with the Fermi surface orbit presented in (c) to (f). At the high symmetry (100) plane, the orbits sit exactly at the zone boundary and therefore for (c) non-SOC case all four orbits are degenerate while for (d) SOC-included case they are doubly degenerate. Meanwhile for orbits sit at the (110) plane, the non-SOC scenario features two spin-degenerate orbits that show four-fold degeneracy only at the zone boundary. While for SOC-included case, the four non-degenerate orbits display a intersecting pattern which results in not only the similar degeneracy protected by crystalline symmetry but also quasi-symmetry protected degeneracies that are not located at the high symmetry directions.

Fermi surface $1^+, 2^-$



Fermi surface $1^-, 2^+$

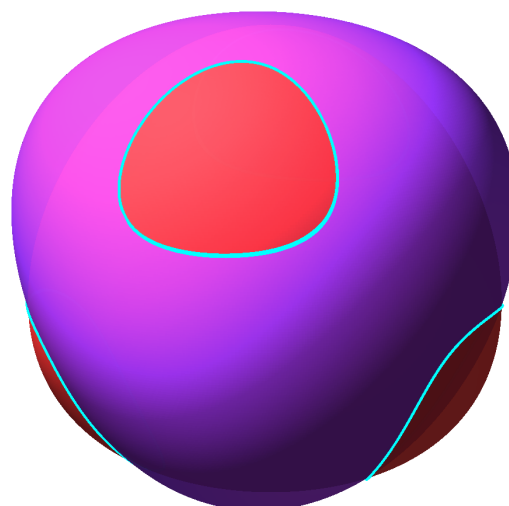


FIG. S5. To clearly demonstrate the intersecting pattern of the Fermi surfaces, here we plot the Fermi surfaces $1^+/2^-$ and $1^-/2^+$, they intersect at the quasi-symmetry protected degenerate rings.

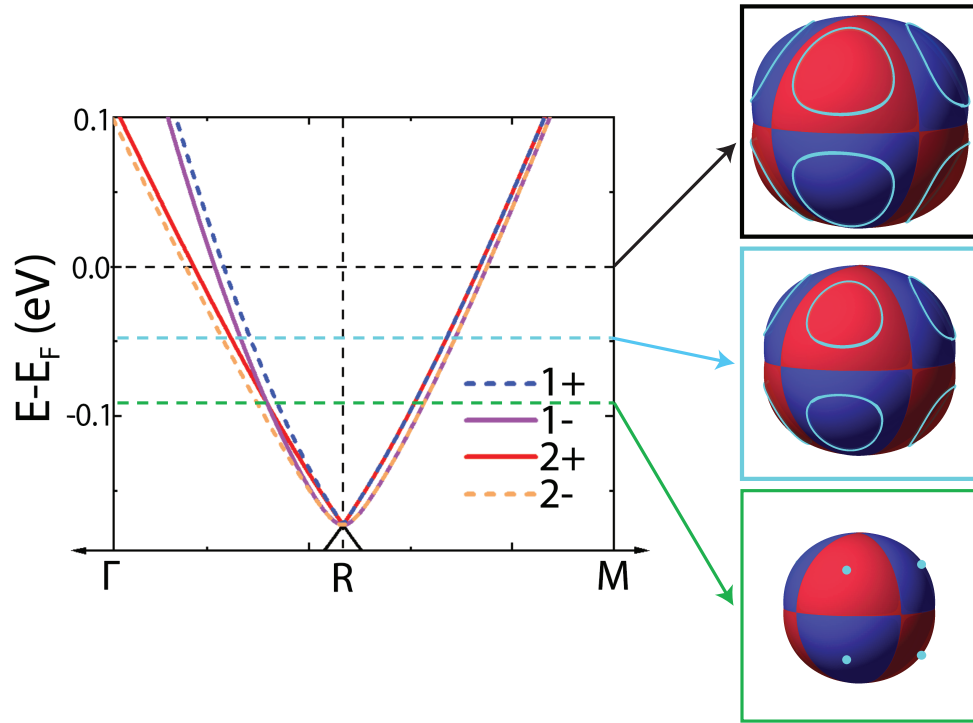


FIG. S6. Fermi energy-dependence of Fermi surfaces 1^+ and 2^+ . Except for the natural reduction of Fermi surface size, the degenerate rings also become smaller with lower Fermi energy. And when the Fermi level locates exactly at the type-II Weyl node, the rings shrink and reshape to eight Weyl points.

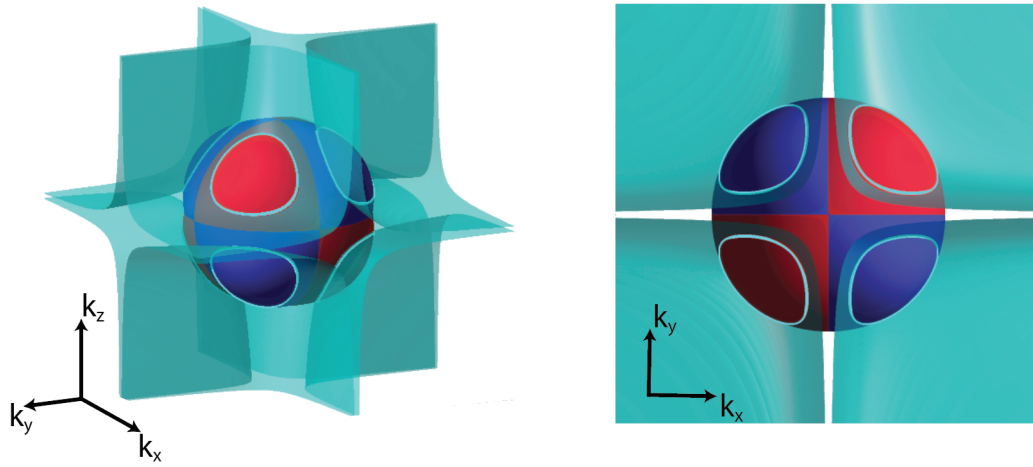


FIG. S7. Fermi surfaces $1^{+}/2^{+}$ and quasi-symmetry protected degenerate planes. They intersect exactly at the eight degenerate rings.

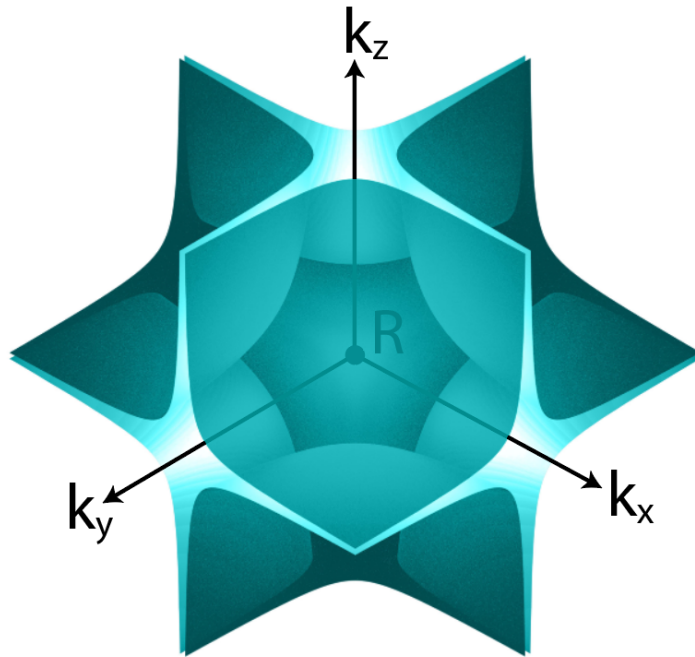


FIG. S8. The eight quasi-symmetry protected degenerate planes.

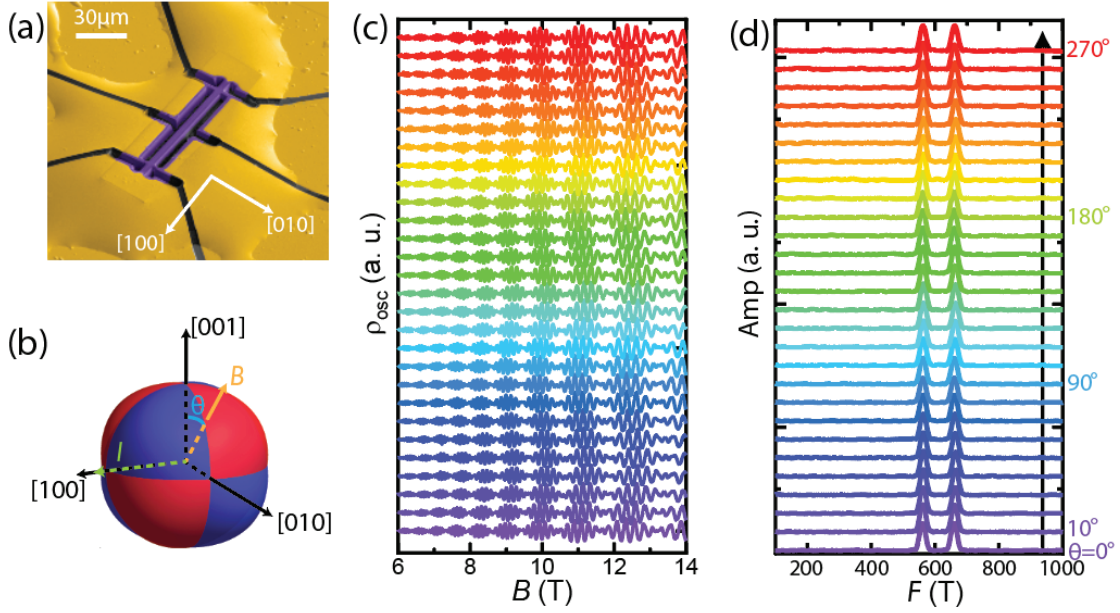


FIG. S9. (a) Scanning electron microscope (SEM) image of device-1. A long bar of a 6 by 6 μm^2 cross section is fabricated with FIB. The golden part stands for the deposited gold thin film for obtaining low resistance ohmic contact and the CoSi crystalline part is colored purple. (b) Illustration of field and current orientation of Shubnikov-de-Hass (SdH) oscillation measurements. θ is defined as the angle between the applied field and [001] axis. (c) SdH oscillations as a function of angle θ . Here $\rho_{osc} = \Delta\rho/\rho_{BG}$ with $\Delta\rho$ the oscillating part of the magnetoresistance (MR) and ρ_{BG} the MR background subtracted by a 3rd-order polynomial function. (d) Fast-Fourier-transformation (FFT) spectrum of SdH oscillations displayed in (c). The two main peaks correspond to two pairs of Fermi surface orbits with same cross section areas.

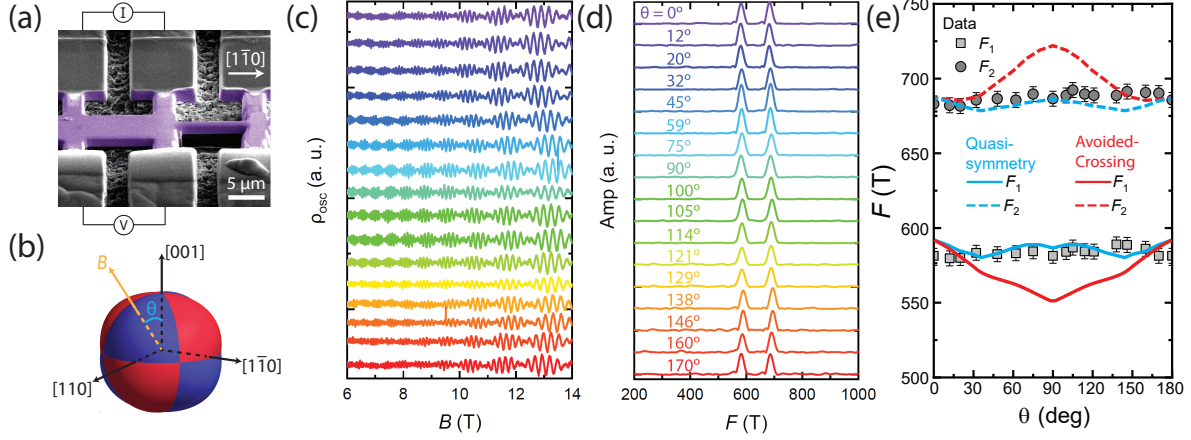


FIG. S10. (a) SEM image of device-2. Here the gold thin film is covered with FIB-deposition of Carbon thin film (grey) for protection of ion beam tail during microstructure fabrication. The current is applied along $[1\bar{1}0]$ axis. (b) Demonstration of field and current orientation of SdH measurements. For device-2 the magnetic field is applied within the $(1\bar{1}0)$ plane, and θ is defined as the angle between the applied field and $[001]$ axis. (c) Angular dependence of SdH oscillations ρ_{osc} . (d) FFT spectrum of SdH oscillations. Again two and only two mean frequencies are observed. (e) Angular dependence of SdH oscillation frequencies and theoretical prediction of both quasi-symmetry and avoided-crossing models. Only quasi-symmetry model successfully reproduced the experimental results.

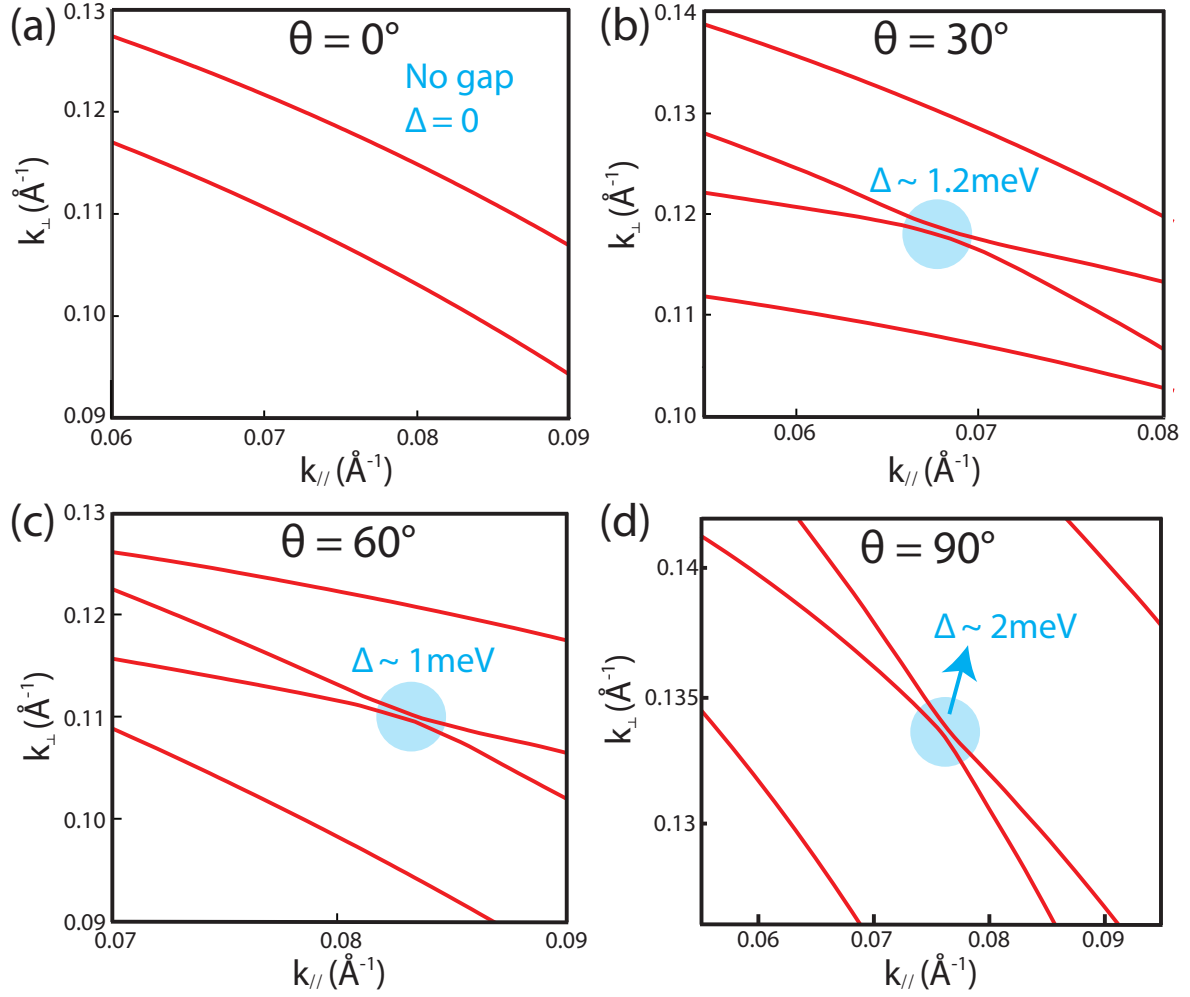


FIG. S11. Fermi surface orbits with field applied along different directions obtained from DFT band structure calculations. Here θ is defined the same as in Fig. S3(a). The largest estimated breakdown gap $\Delta \approx 2$ meV occurs when field is applied along $[110]$ axis ($\theta = 90^\circ$).

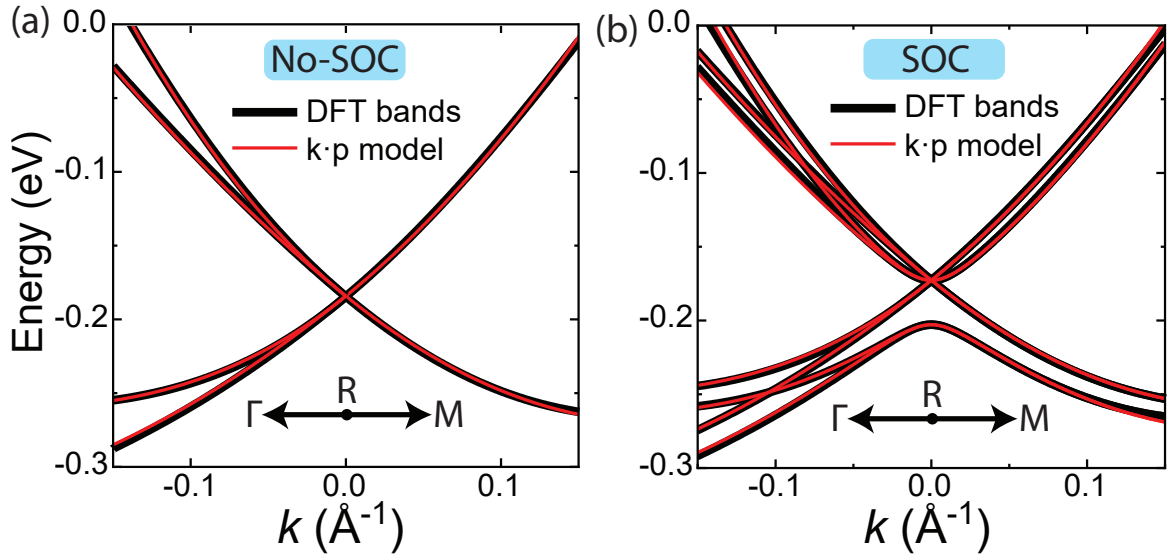


FIG. S12. DFT-calculated Band structures (black) and $k \cdot p$ model fitting (red) around the R -point. (a) The fitting along the $R - M$ line generates parameters C_0, A_1, B_1 for the $\mathbf{k} \cdot \mathbf{p}$ Hamiltonian without SOC. The remaining parameters C_1, C_2, C_3 are obtained for the $\mathbf{k} \cdot \mathbf{p}$ Hamiltonian without SOC along the $R - \Gamma$ line. (b) Fitting the strength of SOC λ_0 for the $\mathbf{k} \cdot \mathbf{p}$ Hamiltonian with SOC (the R -model) along the $\Gamma - R - M$ line.

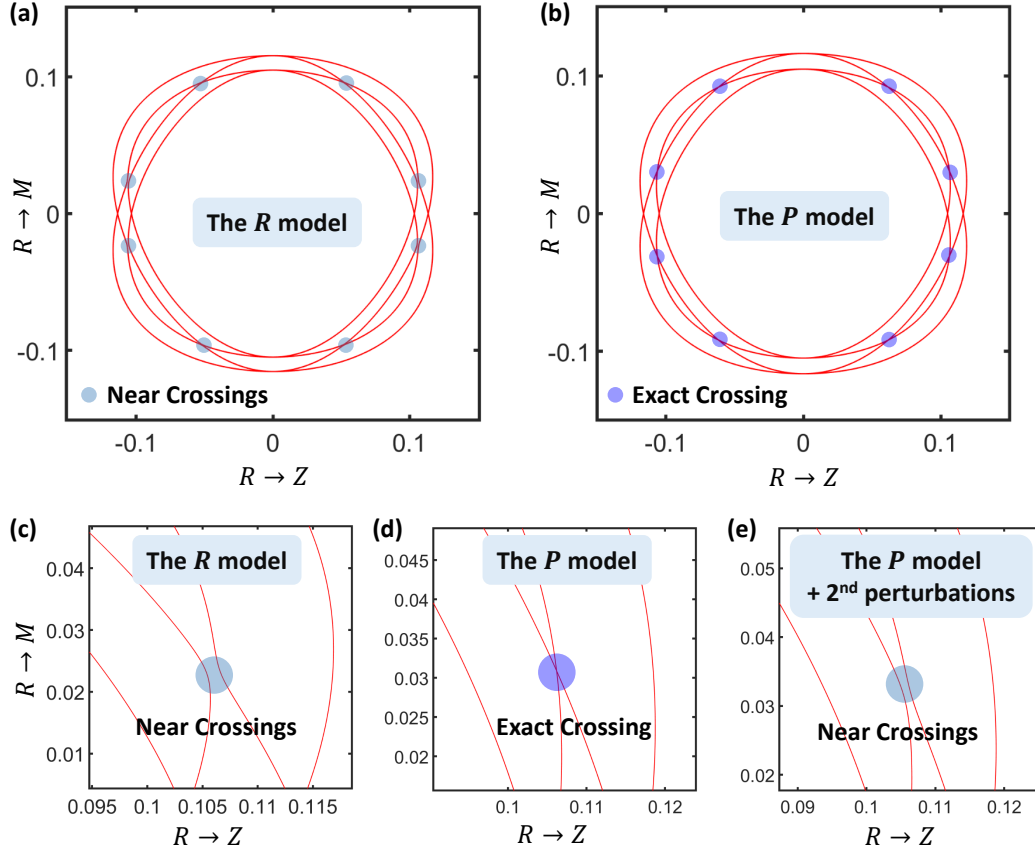


FIG. S13. Fermi surfaces at $E_f = -0.06$ eV in the $\Gamma - R - M$ plane. (a) Fermi surfaces generated from the R -model, eight near crossings are found and marked by light-blue solid circles. As a comparison, the Fermi surfaces for the P -model is shown in (b), which display eight exact crossings (marked by purple solid circles). The zoomed plots for the near/exact crossings are shown in (c),(d) and (e). (c) R -model calculations indicate a very tiny gap for the near crossings. (d) The exact crossings in P -model with only first order perturbation is shown for a comparison, of which the two-fold degeneracy is protected by the quasi-symmetry. (e) After adding the second-order perturbation corrections to the P -model, the quasi-symmetry is broken and thus the exact crossings are gapped. In all figures, the unit for energy is eV and that for momentum is \AA^{-1} .

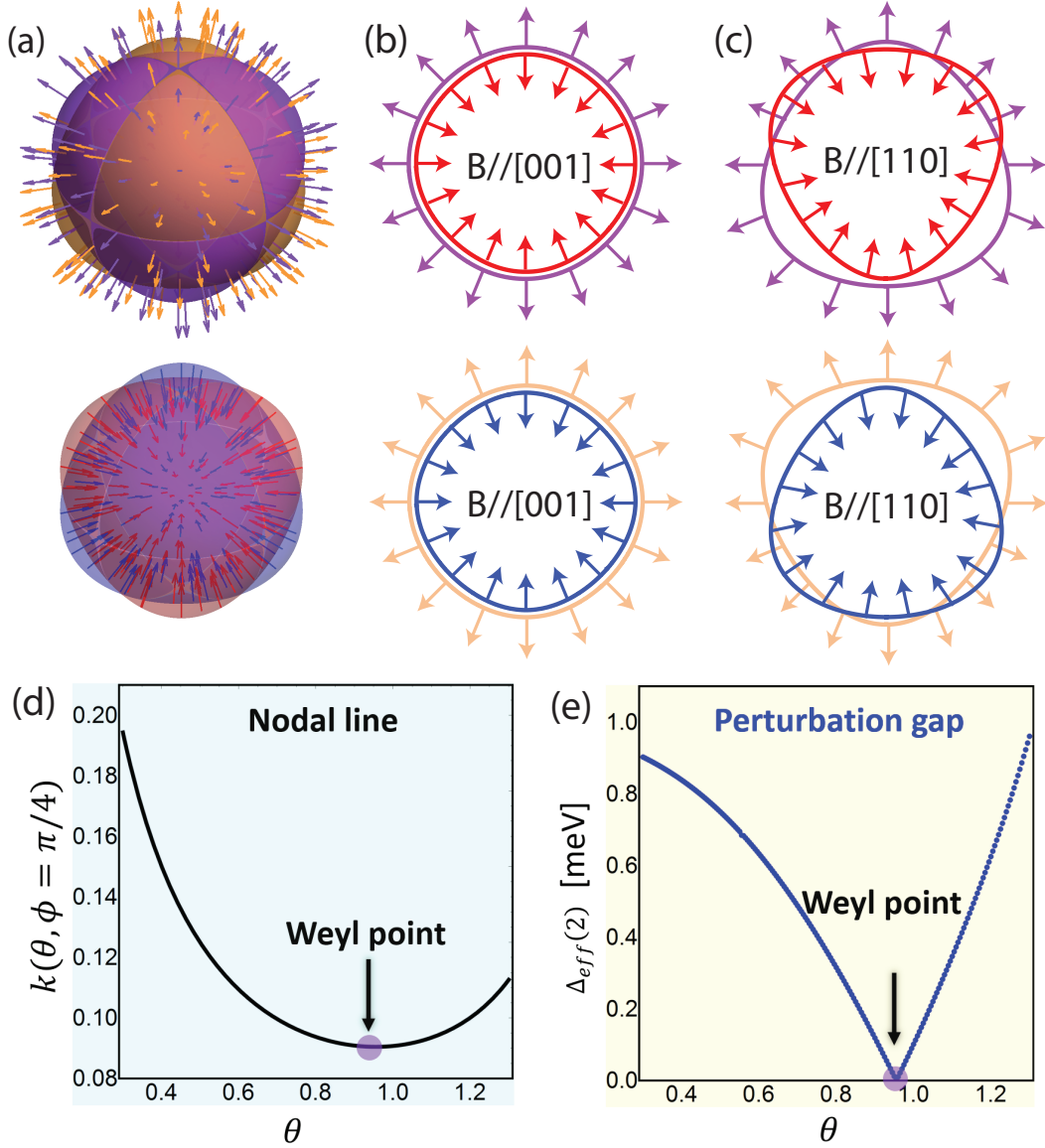


FIG. S14. (a) The spin texture (colored arrow) for all four Fermi surfaces calculated from the P -model. As discussed in the main manuscript, since the spin of the eigen-states is parallel or anti-parallel to the momentum, Fermi surfaces with different spin character(+/-) have opposite spin-polarization at the same momentum. (b) and (c) present the spin texture of Fermi surface orbits with field applied along [001] and [110] direction respectively. (d) Nodal line on the $\Gamma - R - M$ plane with $\theta \in \{0, \pi/2\}$ and $\phi = \pi/4$ obtained by solving $d_z(\mathbf{k}) = 0$ in Eq. (S49). (e) Energy gap on the nodal line caused by the second-order perturbation corrections, $\delta_{eff(2)} = 2\sqrt{(\delta d_x)^2 + (\delta d_y)^2}$, in unit of meV. This gap is resulted from the second-order perturbation which involves the spin-flipping terms. The momentum k is in unit of \AA^{-1} .

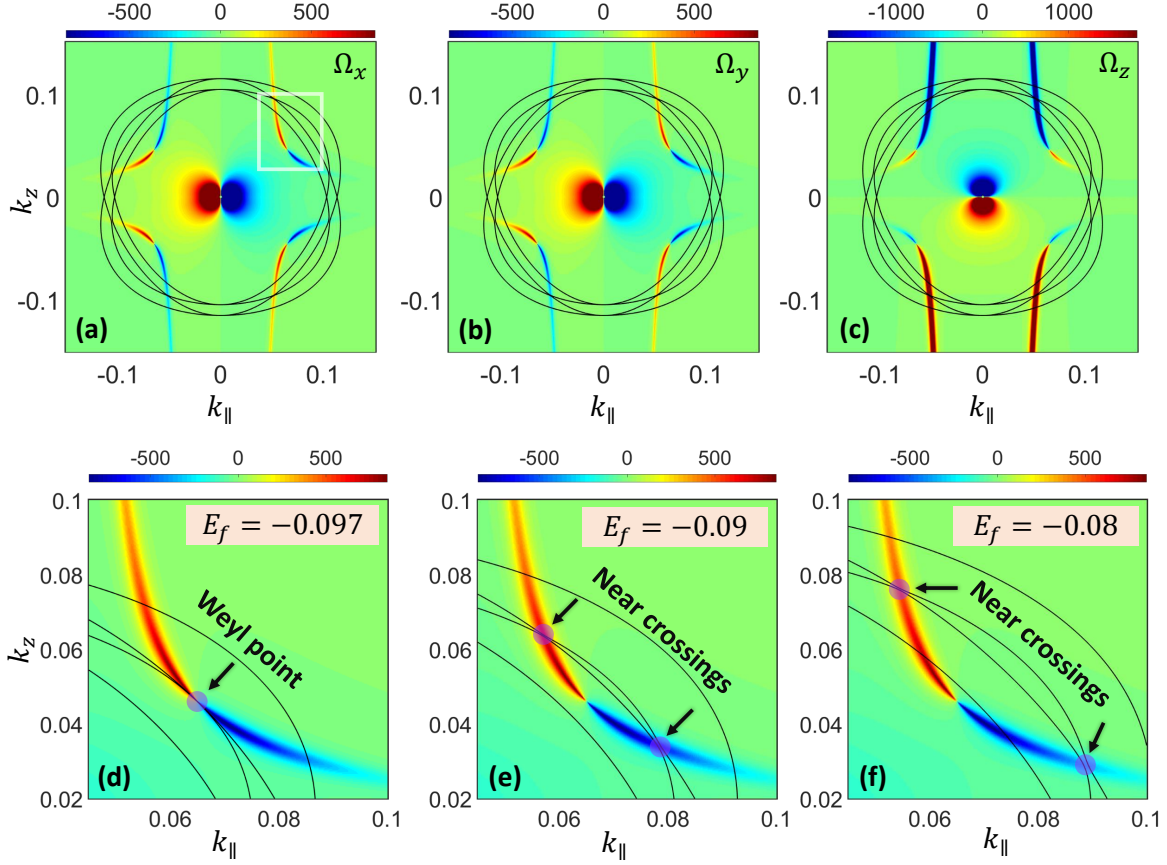


FIG. S15. The Berry curvature distributions around the near crossings on the $\Gamma - R - M$ plane. In (a),(b) and (c), the three component of the Berry curvature ($\Omega_{x,y,z}$) are shown for the the 1^- -band. The black lines stand for the Fermi surface contour with $E_f = -0.06$ eV. The zoomed plot for Ω_x in (a) is shown in (d),(e) and (f), where we compare the Fermi surface flow as the distributions of Ω_x . The Fermi energies are $E_f = -0.097$ eV, $E_f = -0.09$ eV, $E_f = -0.08$ eV for (d), (e), and (f), respectively. The singularity is at the type-II Weyl points, as well as that for the 6-fold degeneracy at the R -point. And the large Berry curvature almost sits at the near crossings (marked by the dark-red solid circles) on the Fermi surface. In all figures, the unit for energy is eV and for momentum it is \AA^{-1} .

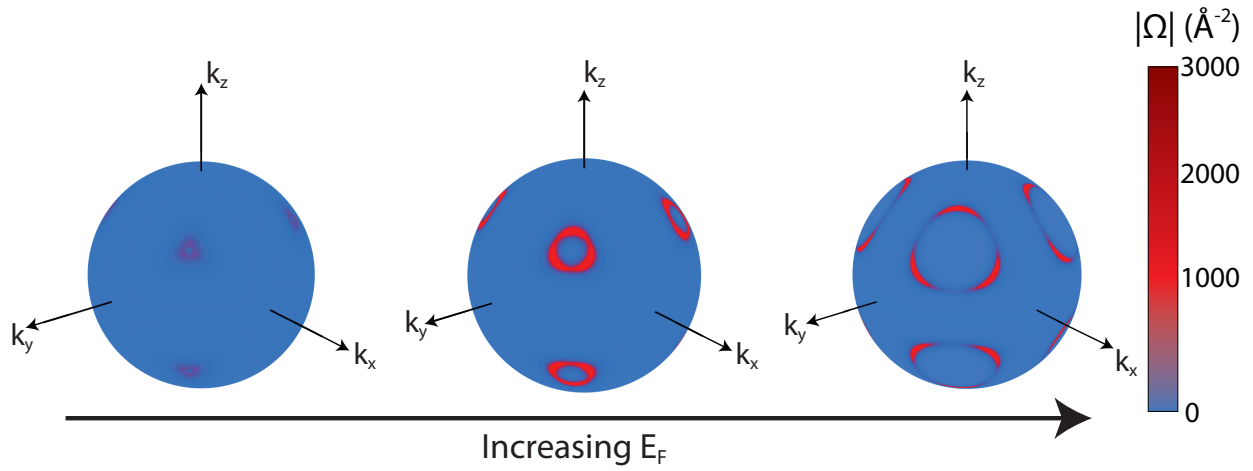


FIG. S16. Energy-dependent Berry curvature in momentum space for the 1^- -band. The large Berry curvature is a direct result of near-degeneracy due to quasi-symmetry.